Modeling a Professional Road Cycling Race To Determine the Fastest Wheel-Tire Combination

TU Delft D.J. de Boer

Abstract

Commissioned for Team DSM, a computational model for professional road cycling races is developed to answer the question: “What is the optimal cycling wheel-tire combination, available to Team DSM in order to ride different road cycling races as fast as possible?”. This model is used to make an approximation of the wind that the cyclist experiences, using race data from Team DSM. Using this wind approximation, race times for different wheel-tire combinations are compared. A sensitivity analysis of the model for the coefficient of rolling resistance, coefficient of drag multiplied with the frontal area, mass and rotational inertia is performed. Taking the error in the measurements of parameters into account, the sensitivity analysis and race time results both point to the “C60 tubeless” wheel-tire combination to be the fastest combination out of the available wheel-tire combinations to Team DSM. If the weight of a C36 wheel-set was reduced, this wheel set could outperform the C60 wheel-set on mountainous race courses.

Contents

1. Introduction

This thesis is written for Team DSM in order to determine the fastest wheel-tire combination for races. Team DSM is a professional road cycling team. Professional sports have been shown to increase the participation levels of amateur sports [1], [2]. Heinen [3] found that commuters are much more likely to cycle to work when they have a positive attitude towards cycling. In addition to that, professional sports are also a driver of technological and medical innovation [4], [5]. This is important because cycling in general can play an influential role in general population fitness and climate change now, and in the future. Increased awareness of the effects of using fossil fuels on our climate and well-being calls for more sustainable modes of transport. Cycling is a healthy and inexpensive form of transport, is environmentally sustainable and has low levels of air and noise pollution [6, 7].

Professional road cycling is a game of marginal gains. In this sport, great effort and funds go to determining what the fastest possible bike-setup is. A professional cycling team receives different components for the bikes they use during a season, from different sponsors. This includes different rims, time-trial bike frames, regular road bike frames, sets of gears, tires, helmets, skin-suits, other clothing and more. The model described in this thesis compares the performance of different cycling wheel-tire combinations, to achieve the best road cycling race performance.

Professional cycling has five Olympic disciplines, namely triathlon, track cycling, BMX, mountain biking, and road cycling racing. This thesis will focus on road cycling racing, which in turn has three disciplines. These disciplines are the individual time-trial, team time-trial, and the road race. During a time-trail, the goal is to cross the finish line in as little time as possible. In the individual time-trail, the race is relatively short and the cyclist has to complete the course alone. During a team time-trial, the cyclists on one team can cooperate by drafting. In road cycling, a peloton is present. The peloton is the largest group of cyclists in that race. It consists of multiple different teams and can be more than 200 cyclists in size. In road cycling, the peloton performs a group start and the cyclist who crosses the finish line first, wins. During the race, smaller groups can try to "break away" from the peloton in order to try to stay ahead of the peloton for the remainder of the race. Road cycling races are longer (150-200km) than time-trials (5-50km).

Team DSM mostly participates in time-trials and road cycling races. There are a multitude of models that describe the performance of a cyclist during time-trials ([8, 9, 10, 11, 12, 13, 14, 15]), where this is not the case for road cycling races. A time-trail is more straightforward to evaluate than a road cycling race. During a time-trial, the cyclist benefits from a pacing strategy [16, 17, 18]. This means that the pace (and power output) can be optimized or predicted. During a road cycling race however, the cyclist is dependent on the speed of the peloton and will not be using a maximum amount of energy during the entire race. The cyclist will have moments of sprinting and moments of rest while moving through the peloton. In addition to this difference in pacing strategy, another unknown factor in road cycling races compared to time-trials is drafting. A time-trial is a solitary affair, where the wind experienced can be relatively predictable. The presence of and movement through a peloton makes a road cycling race very different in that sense. The air, or "wind" that a cyclist encounters while cycling in a peloton will not be equivalent to the wind experienced when cycling alone.

Before every race, Team DSM decides which cycling parts to use to win the race. Course and weather can influence which components are most efficient to cycle with [11, 8, 15]. It is well known that drafting in a peloton reduces the aerodynamic drag experienced by cyclists ([19, 20, 21, 22, 23, 24, 25]). It is not clear, though, what effect drafting has on the choice of equipment selected for a cycling race. Aerodynamically better components are heavier than components that are less aerodynamically beneficial. A very clear example of this is cycling wheels. A wheel with a deeper rim is aerodynamically more efficient, but costs more energy when accelerating or ascending than a lighter wheel. There is a general consensus in the

professional cycling world that a shallow rim is better for mountainous races and a deep rim is better for flatter races. There is no research available which actually investigates this assumption. When the drag reduction from the peloton is taken into account, the tipping point of when to start using different components might shift. The model described in this thesis takes the effect of the drag reduction from a peloton into account to determine the optimal wheel-tire combination for a race.

In this thesis, the following research question is answered: "What is the optimal cycling wheel-tire combination, available to Team DSM in order to ride different road cycling races as fast as possible?". In order to answer this question, the following sub-questions are used.

- What is the influence of change in the inertia, mass, rolling resistance and aerodynamic drag on the wheel-tire combination choice?
- How reliable are the results of the simulation?

1.1 Cycling Wheels and tires

In this thesis, the differences between different wheels and tires are discussed. To do this, it is important to understand these differences. Figure 1.1 shows cross sections of different tire constructions. The "clincher" system is a relatively common tire in commute-bicycles. This system has an inner tube that is held in place by the outer tire, which in turn makes contact with the road. The "tubular" system is the first of the 2 systems that Team DSM uses. The tubular tire consists of a tube sown into an outer tire that is glued to the rim. The "tubeless" system does not use an inner tube and is sealed with a combination of pressure and "sealant". Sealant is a glue that is injected into the cavity formed by the tubeless tire and the rim. The general consensus is that a tubeless tire has a lower rolling resistance than tubular tires due to the absence of friction between the inner tube and the outer tire [26, 27, 28]. The rims that support tubeless tires are generally slightly heavier than the rims that are used for tubular tires.

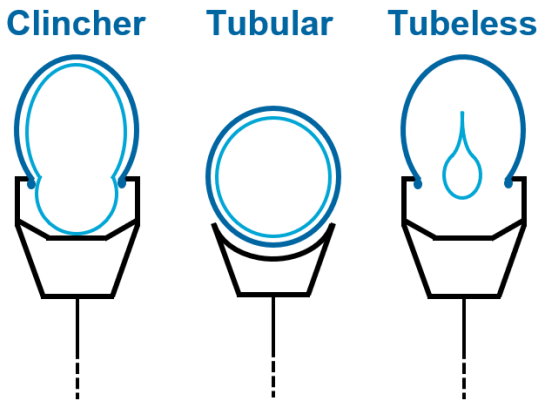

Figure 1.1: Figure that shows a cross-section of 3 available tire types for bicycles. On the left, the "clincher" tire-type can be seen. This is a common type used in city bicycles and also older road bicycles. This is a construction where an inner tube is kept in place by the outer tube, which hooks behind the rim. The middle tire-type is the "tubular" tire-type. This tire consists of one piece which includes an inner tube and outer tube. This outer tube is glued to the rim. The right-most tire-type is the "tubeless" tire-type. This tire-type doesn't use an inner tube, but relies on "sealant" to seal the sides of the outer tire to the rim.

Rims also come in different rim depths. Figure 1.2 illustrates what is meant by rim depth. A deeper rim depth means that more of the wheel consists of rim and it can be seen that a deeper rim has a larger cross-sectional area. A deeper rim depth is beneficial for aerodynamics due to the longer attachment of airflow to the wheels and due to the "sailing effect". This sailing effect uses the lift that is generated when the wind arrives at a wheel at an angle. Due to the larger surface of the wheel, a low pressure field originates on the lee side of the wheel. This underpressure effectively pulls the wheel forward. The sailing effect is further explained in the literature study [29]. Team DSM uses 3 rim sizes, namely "C36", "C50" and "C60" rims. These are different rim depths and are available as tubular or tubeless. The C36 is the shallowest rim with a rim depth of 36mm and the C60 is the deepest rim, with a rim depth of 60mm.

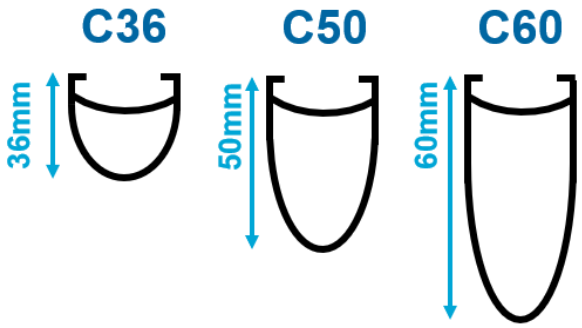

Figure 1.2: Figure that shows the shape of the cross-section of a rim for different rim-depths. It can be seen that a deeper rim has a larger cross-sectional area.

In Chapter 2, the methodology of this thesis is explained. In Chapter 3, the process to attain the rotational inertia of the cycling wheels is explained. In Chapter 4, the numerical methods are explained, where the choices in the modeling process are justified. In Chapter 5 the error estimation and sensitivity analysis of the model are shown. In Chapter 6, the results from the simulations are presented. Chapter 7 contains the discussion of the results shown in Chapter 6. Chapter 8 contains the conclusions and future recommendations for this model.

2. Methodology

In order to answer the research question, a force balance equation of a cyclist on a bicycle is used. The bicyclist and bicycle are modeled as a point mass and 1 rotating disc that rotates proportionally to the speed of the cyclist, that can move over an elevation profile while obeying Newton's second law. In order to do this, it is assumed that wind is 1-directional and always parallel to the cycling direction, that the cyclist can be modeled as a point mass, that the 2 wheels can be modeled as 1 disc with the inertia of 2 wheels and that any forces outside of the 2D-plane are not of a significant effect on the outcome of this model. In this chapter, the model used is explained in detail. Resulting from these details, the steps that need to be undertaken before the cyclist can be simulated are explained.

2.1 Forces on the cyclist

In Figure 2.1, a free body diagram of the bicycle (and the cyclist) can be seen, as used in the model. The forces in the figure are not drawn to scale. In the figure, the propulsion force (F_p), normal force (F_n), gravitational force (F_{grav}), Braking force (F_b), rolling resistance force (F_r), drag force (F_d), wheel bearing resistance force (F_w) and the slope of the road (α) can be seen. The resulting force of F_n and F_{grav} is not shown in the figure and is called F_g. All forces act on the center of mass of the bicycle, since the bicycle is modeled as a point mass. The variables and constants used to describe these forces are not all immediately available and some had to be acquired. In this section, each force is explained in detail. After this, Table 2.1 shows for each parameters whether this is known, received from Team DSM or acquired by other means.

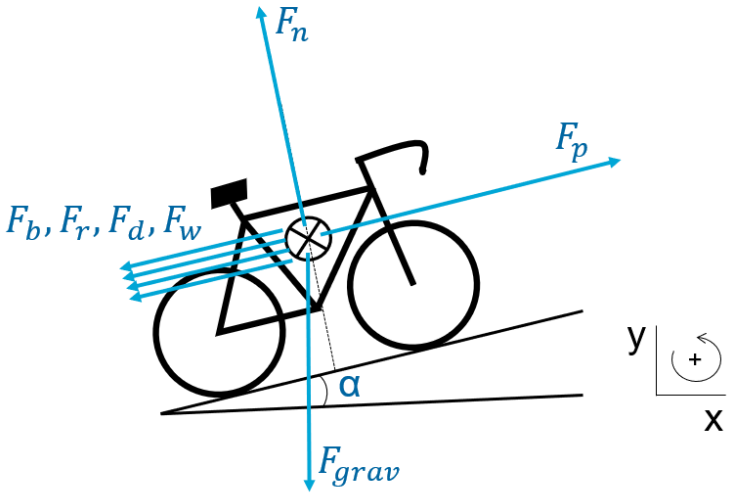

Figure 2.1: Free body diagram of the bicycle-cyclist combination that is used for the model in this thesis. The Propulsion force (F_p), Normal force (F_n), Gravitational force (F_{grav}), Braking force (F_b), Rolling resistance force (F_r), Drag force (F_d), Wheel bearing resistance force (F_w) and the slope of the road (α) can be seen. All forces act on the centre of mass of the bicycle, since the bicycle is modeled as a point mass. The forces are not drawn to scale.

Using Figure 2.1, the sum of the forces is set as in Equation 2.1. Here, $F_g = F_n + F_{grav}$ and ΣF is the sum of the forces on the cyclist. When riding downhill, F_g is negative, effectively pushing the cyclist forward. When riding uphill, F_g is positive, effectively pulling the cyclist back. F_b is the braking force when squeezing the brakes on the bicycle. Each component of the sum of the forces is further expanded on in this chapter.

$$\Sigma F = F_p - (F_d + F_w + F_r + F_g + F_b) \tag{2.1}$$

In order to model the bicycle-cyclist system, Newton's second law is used ($\Sigma F = ma$), where m is the mass of an object and a is the acceleration of the object. With this, the acceleration of the cyclist is calculated. This does not include the inertia of different wheels on the performance of the cyclist. So in order to be able to incorporate the effects of rotating wheels as well, $\Sigma\tau = I\alpha$ is used. Here, $\Sigma\tau$ is the sum of the torques around the object, I is the mass moment of inertia of the object and α is the angular acceleration of the object. A no-slip condition of the tires with the ground is assumed. Using this, the rotational acceleration of the wheel is directly proportional to the radius. ΣF is expressed in Equation 2.2, where r is the radius of the wheel and I is the rotational inertia of both wheels ($I = I_{front} + I_{rear}$).

$$\Sigma F = a(m + \frac{I}{r^2}) \tag{2.2}$$

The equation for the aerodynamic drag force can be seen in Equation 2.3. Here, ρ is the density of air, $C_D A$ is the drag coefficient multiplied by the frontal area, V is the speed of the cyclist and V_{wind} is the wind speed, parallel to the cycling direction. Figure 2.2 shows what it means when V_{wind} is parallel to the cycling direction. This figure shows the positive directions for the speeds mentioned in Equation 2.3.

$$F_d = sgn(V + V_{wind})\frac{1}{2}\rho C_D A(V + V_{wind})^2 \tag{2.3}$$

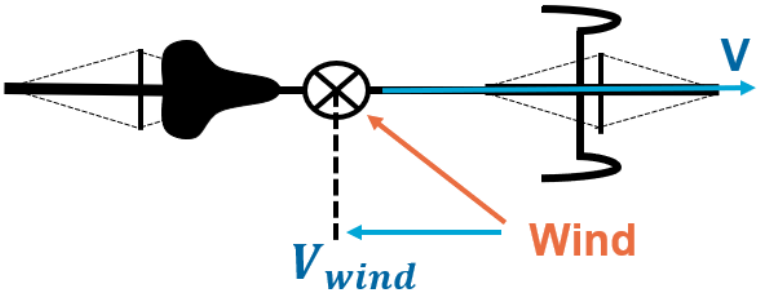

Figure 2.2: Figure in which can be seen that for the case of the wind-speed (V_{wind}), only the component parallel to the cycling direction is considered. This means that the side-forces are not taken into account. It can be seen that the "real" wind comes in at an angle and V_{wind} is the component in the parallel direction of V

The gravity force depends on the angle of the road and the mass of the cyclist. The equation for the gravity force acting on the cyclist can be seen in Equation 2.4. Here, m is the total mass of the cyclist and the bicycle lumped together, g is the gravitational constant and θ is the angle of the road. The angle of the road is defined as $\theta = tan^{-1}(\alpha)$.

$$F_g = mgsin(\theta) \tag{2.4}$$

The rolling resistance is dependent on the type of tire, road surface and the tire pressure. This is captured by the coefficient of rolling resistance (C_{rr}). The rolling resistance can be seen in Equation 2.5. Here, C_{rr} is the coefficient of rolling resistance.

$$F_r = C_{rr} mgcos(\theta) \tag{2.5}$$

The wheel bearing resistance is found in [30], where it is found from experimental results that the torque around a wheel can be expressed as: $T = 0.015 + 0.00005N$. Here, T is the torque and N is the rotational velocity in RPM. Using $F = \frac{T}{r}$ and $N = \frac{V}{2\pi r}$, this is written into an equation of a resisting force dependent on cycling speed and the radius of the wheel (Equation 2.6). Here r is the radius of the bicycle wheel and V is the speed of the cyclist.

$$F_w = \frac{0.015}{r} + \frac{0.00005V}{2\pi} \tag{2.6}$$

The propulsion force is the force caused by the power of the cyclist that is delivered to the pedals of the bicycle. The propulsion force can be seen in Equation 2.7. Here, P is the power delivered by the cyclist and V is the speed of the cyclist. Team DSM has data on the power and speed of each individual cyclist. Using this equation, this data is translated to a force acting on the cyclist.

$$F_p = \frac{P}{V} \tag{2.7}$$

The braking force is a force that is self-defined, dependent on the speed of the cyclist in the data made available by Team DSM. In the modeling process (Chapter 4), turn identification for the braking force is further discussed. For now, it can be assumed that the cyclist applies a braking force close to a turn. The braking force is a force, based on constant deceleration, where the difference between the current speed and the cornering speed is used, as can be seen in Equation 2.8. Here, m is the mass of the cyclist and the bicycle, ΔV is the difference between the cornering speed and the speed a distance (s) from the turn.

$$F_b = m\left(\frac{\Delta V}{s}\right) \tag{2.8}$$

In order to forward simulate the cyclist, numerical integration over time is used. Details of this integration can be seen in the section on error estimation in Chapter 4.

2.2 Parameter availability

In the previous section, all variables and constants are shown. Table 2.1 shows which of these parameters is known, received from Team DSM or otherwise acquired. In this table, it can be seen that all parameters but the rotational inertia of the wheels (I) and the wind speed (V_{wind}) are known or received from Team DSM. The next sections elaborate on the acquisition of the rotational inertia and the wind speed.

	Known	Received from Team DSM	Otherwise acquired
Gravitational constant (g)	x		
Air density (ρ)	x		
Mass of bicycle and cyclist (m)		x	
Rotational inertia wheels (I)			x
Radius of Wheels (r)		x	
Frontal area (A)		x	
Coefficient of drag (Cd)		x	
Coefficient of rolling resistance (C_{rr})		x	
Speed (V)		x	
Angle of the road (θ)		x	
Power (P)		x	
Wind speed (V_{wind})			x

Table 2.1: Table which shows for every parameter whether it is known (common knowledge), received from Team DSM or otherwise acquired. Attainment of parameters is be done either through calculation or experimental work.

2.2.1 Rotational Inertia

The rotational inertia affects the acceleration and deceleration of the cyclist. In races where a lot of speeding up and slowing down occurs, a wheel with a lower rotational inertia is beneficial if all other parameters are equal. However, in reality, a heavier wheel is usually more aerodynamic than a lighter wheel. In order to determine the rotational inertia, an experiment is set up which is further worked out in Chapter 3.

2.2.2 Wind speed

A difference between an individual time trial and a road cycling race, is the presence of a peloton. This large group of cyclists is "a competitive system composed of riders with multiple objectives that serve to advance riders' overall competitive goals" [31]. This peloton consists of groups of up to 200 cyclists. Blocken [25] simulated tightly packed pelotons in a wind tunnel and with Computational Fluid Dynamics (CFD). In both cases, the authors report a drag reduction of up to 96%. Druenen [32] shows that more than 12% power savings can be achieved while drafting uphill, where speeds are low. This shows the importance of modeling the presence of a peloton when selecting bicycle components for road cycling races. To capture the effects of the presence of the peloton, the variables and constants defined in Table 2.1 are used to calculate an estimation of the wind speed experienced by a cyclist. The power, slope, speed and mass are cyclist specific. All other parameters are assumed to be equal between all cyclists. After the rotational inertia of the wheel is found, these parameters are used to calculate a cycling-specific wind estimate. This is done by solving for the wind speed (V_{wind}) in the force balance equation since all the parameters except the wind speed are known. Equation 2.1 is written into Equation 2.9 to express the drag force (F_d) as an expression of known forces.

$$F_d = F_p - (a(m + \frac{I}{r^2}) + F_w + F_r + F_g + F_b) \tag{2.9}$$

Combining Equation 2.9 and Equation 2.3, results in Equation 2.10.

$$sgn(V + V_{wind})\frac{1}{2}\rho C_D A(V + V_{wind})^2 = F_p - (a(m + \frac{I}{r^2}) + F_w + F_r + F_g + F_b) \tag{2.10}$$

To solve the non-linear equation that is a result of Equation 2.9, the Python package scipy.optimize.fsolve is used [33]. This process needs a guess in order to pick the correct root. This process is explained in more detail in Chapter 4. To obtain this initial guess, Equation 2.11 is used as an alternative drag force.

$$F_d = \frac{1}{2}\rho C_D A(V + V_{wind})^2 \tag{2.11}$$

This alternative drag force is then substituted in Equation 2.9 and solved for V_{wind}. Here, it is chosen to take the positive value of the quadratic solution resulting from the substitution. When the negative solution is chosen, only negative wind-speed solutions can be found. This results in Equation 2.12. Whenever the root shown in Equation 2.12 becomes imaginary, this is assumed to be 0 for the estimation of the solution of the nonlinear equation.

$$V_{wind} = \sqrt{\frac{2(F_p - (a(m + \frac{I}{r^2}) + F_w + F_r + F_g + F_b))}{\rho C_D A}} - V \tag{2.12}$$

With this solution, a cyclist-specific estimation of the experienced wind speed is attained.

2.3 Comparing different wheels

After the rotational inertia and the wind speed are determined, different components are compared. Assuming that the estimated wind speed is equal for each component, the model is run with the parameters of the original set of wheels. This produces a simulated race time. After this first run, the parameters are changed to represent changing a wheel-tire combination. This configuration is then run for the same power and wind profile to produce a race-time. This is done for each desired wheel-tire combination. After that, the different race times are compared in order to evaluate which wheel-tire combination would have been faster. The swap of wheels will affect the values for the rotational inertia of the wheels, weight of the bicycle and the $C_D A$ of the bicycle.

3. Wheel rotational inertia

3.1 Introduction

This chapter shows the process for determining the rotational inertia of the cycling wheels used by Team DSM. First, the measurement method is described. Second, the measurement protocol and result processing are explained. Finally, the results of the inertia measurements are presented.

3.2 Pendulum Method

Since the model is 2-dimensional, only the rotational inertia of the cycling wheels needs to be measured. The inertia over other axes is considered to be negligible. When looking at figure 3.1, the torque around point the origin (O) for a physical pendulum in space is the force perpendicular to the direction from O to the center of mass(CM), multiplied by the distance over between O and CM (L), which is the arm over which the force works. This results in equation 3.1. Here, τ is the torque around O, m is the mass of the pendulum, g is the gravitational constant and θ is the angle the pendulum makes to the neutral axis.

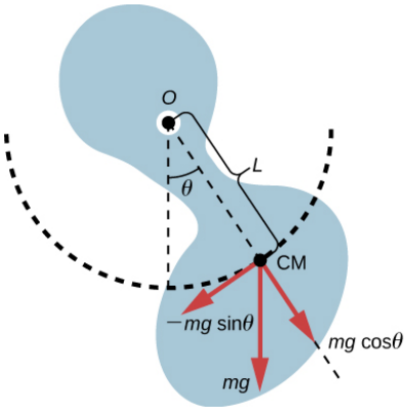

Figure 3.1: A physical pendulum in space. In this case, the pendulum is oscillating around point O. θ depicts the angle of the line made between CM and O and the resting position of the pendulum. The force mg is acting on CM, which can be decomposed in a force in line between O and CM and a force perpendicular to this line. L depicts the distance between O and CM. Original image from Lumenlearning.com, by OpenStax [34] under CC BY 2.0

$$\tau = -Lmgsin(\theta) \tag{3.1}$$

The torque around O can be expressed by the angular acceleration (α) times the inertia of a body around O, ($\tau = \alpha I_o$). Here, I_o is the inertia of the body around O. Assuming that $sin(\theta) = \theta$ for small angles and using this relation for the torque, Equation 3.2 can be expressed.

$$\alpha I_o = -Lmg\theta \tag{3.2}$$

Using that α can also be written as $\frac{d^2\theta}{dt^2}$, the angular acceleration can be written as Equation 3.3

$$\frac{d^2\theta}{dt^2} = -\left(\frac{mgL}{I_o}\right)\theta \tag{3.3}$$

This is a second-order differential equation, for which the standard solution for $\frac{d^2\theta}{dt^2} = -b\theta$ is used, with b being a constant. This gives $\theta(t) = cos(\omega t + \phi)$ with $\omega^2 = b$. This results in an expression for the angular speed (ω), as can be seen in Equation 3.4

$$\omega = \sqrt{\frac{mgL}{I_o}} \tag{3.4}$$

Using this, I_o can be expressed as a function of ω, which can be seen in Equation 3.5

$$I_o = \frac{mgL}{\omega^2} \tag{3.5}$$

Now, using the Parallel Axis Theorem (Equation 3.6), the moment of inertia around the center of mass of the wheel (I_{cm}) can be expressed as in Equation 3.7. The centre of mass of the wheel lies in the middle of the wheel's axle.

$$I_o = I_{cm} + mL^2 \tag{3.6}$$

$$I_{cm} = \left(\frac{mgL}{\omega^2}\right) - mL^2 \tag{3.7}$$

To do these measurements, the wheel is suspended on a point contact where it can freely oscillate when pushed. A convenient location for this is the inside of the rim. A stiff, round metal rod is used to lay the rim on during measurements. Here, a relatively small radius for this rod is ideal, to come as close to a point contact as possible, while still maintaining enough stiffness so the rod does not have large-amplitude vibrations when the wheel is made to oscillate. A "Silicon Sensing Systems C42-02" angular rate sensor is used [35] to measure the angular speed. Figure 3.2 gives an illustration of where the sensor is placed.

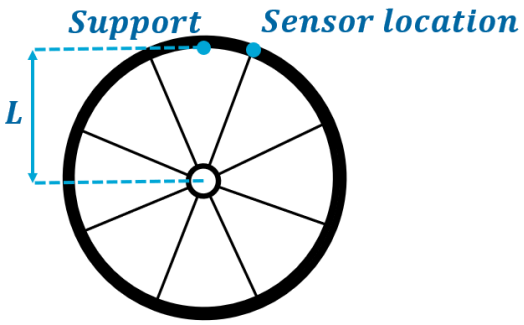

Figure 3.2: Illustration of the pendulum length L, from the axle to the support location, and the location where the angular rate sensor is placed

Extra attention is paid during these measurements to limit oscillation in the sideways direction when pushed. By sideways, motion outside of the plane of the rolling direction is meant. When the angular speed is measured, the moment of inertia can be solved for (Equation 3.7).

3.2.1 Practical considerations for the pendulum method

L is the distance between the axis of rotation of the wheel and the inner radius of the rim. m is the mass of the rim, or the rim and the tire if applicable. The mass is measured, using a scale that is accurate to $1g$. When a tire is present on the rim, it is inflated to 7 bars of pressure. The angular speed sensor used, is located in the same location for each rim. This is on the edge of the rim, in line with the spoke that is closest to the rotation point of the pendulum.

3.2.2 Measurement Method Decision

Appendix A contains an alternative measurement method. A comparison is made between the method used ("pendulum method") and an alternative method ("spinning method") considered with respect to the expected error in this measurement. The expected error in the rotational inertia is $2.44 \cdot 10^{-4}$ and $1.87 \cdot 10^{-4}$ for the pendulum method and the spinning method, respectively. This difference in error was not found to be convincing enough with respect to the other uncertainties surrounding the spinning method, where would be difficult to know what the influence of bearing friction and repeatability would be..

3.3 Protocol

Team DSM has a number of possible wheel-tire combinations available. Team DSM has 3 different rims (C36, C50, C60), which are available in a tubular (Tube) version and a tubeless (TL) version. Team DSM also has 3 different tire widths available (26mm, 28mm and 30mm). The rear wheel has a cassette that is universal for all rims and tire types. Since the tires and cassettes are interchangeable, not all wheel-tire combinations are measured explicitly. Table 3.1 shows which wheel-tire combinations were explicitly measured. The tire and cassette are located at the same location, relative to the axle of the rim in the rotation plane, for each wheel-tire combination. That is why it is assumed that the contribution to the inertia and mass due to a tire is the same over different rims. The same assumption is made for the cassettes. In Table 3.2, the mass of each wheel-tire combination can be seen.

	Tube		Tubeless	
	C36 Front	C36 Rear	C36 Front	C36 Rear
Tire 26mm	x			
Tire 28mm	x			
Tire 30mm	x			
Only rim			x	

	Tube		Tubeless	
	C50 Front	C50 Rear	C50 Front	C50 Rear
Tire 26mm	x		x	
Tire 28mm	x	x	x	
Tire 30mm	x		x	
Only rim	x	x	x	

	Tube		Tubeless	
	C60 Front	C60 Rear	C60 Front	C60 Rear
Tire 26mm				
Tire 28mm			x	
Tire 30mm				
Only rim	x		x	

Table 3.1: Table that shows an "x" in every wheel-tire combination tested while doing measurements to attain the rotational inertia of the wheel-tire combinations and also just the rim. Using the knowledge that the tires are in the same location relative to the axis of the wheel in every situation, makes it possible to calculate the rotational inertia of all the possible wheel-tire combinations.

	Tube		Tubeless	
	C36 Front	C36 Rear	C36 Front	C36 Rear
Tire 26mm	979g	1315g*	1068g*	1394g*
Tire 28mm	1015g	1341g*	1087g*	1413g*
Tire 30mm	1042g	1368g*	1093g*	1419g*
Only rim	663g*	989g*	748g	1074g*

	Tube		Tubeless	
	C50 Front	C50 Rear	C50 Front	C50 Rear
Tire 26mm	1050g	1376g*	1139g	1465g*
Tire 28mm	1087g	1413g	1158g	1484g*
Tire 30mm	1114g	1440g*	1164g	1490g*
Only rim	735g	1054g	819g	1145g*

	Tube		Tubeless	
	C60 Front	C60 Rear	C60 Front	C60 Rear
Tire 26mm	1130g*	1456g*	1216g*	1542g*
Tire 28mm	1156g*	1482g*	1232g	1558g*
Tire 30mm	1183g*	1509g*	1241g*	1567g*
Only rim	804g	1130g*	896g	1222g*

Table 3.2: This table shows the weight in grams for each rim-tire combination and of just the rim, of which the angular speed was measured to determine the rotational inertia. All weights marked with an asterisk (*) are calculated and not explicitly measured

The test protocol is defined as follows:

1. For each type of wheel, the inner rim radius is measured, these radiuses of the rims can be seen in Table 3.3.
2. If there is a rim on the tire, the tire is inflated to 7 bar of pressure.
3. The rim-tire combination is then weighed.
4. The sensor is stuck to the rim, with the top of the sensor aligned with the rim, in line with the spoke that is closest to the suspension point.
5. The wheel is then pulled out in the rotation direction and let go, starting the oscillation.
6. After 15 seconds of measurement, the measurement is stopped.
7. This is repeated for each wheel-tire combination measured.

In Figure 3.3, the experimental setup can be seen. The rim is restricted by the wooden structure visible in the figure, to be only able to oscillate in the riding direction. In Figure **??**, a close-up of the measurement device for angular velocity can also be seen. During testing, the rim experienced some friction against the sides of the wooden structure. This friction is compensated for by fitting a decaying sinusoid over the measurement data.

	Inner rim radius
C36	285mm
C50	272mm
C60	261mm

Table 3.3: Table that shows the inner radius of each available rim. This inner radius is the pendulum length, used to determine the rotational inertia of the wheel.

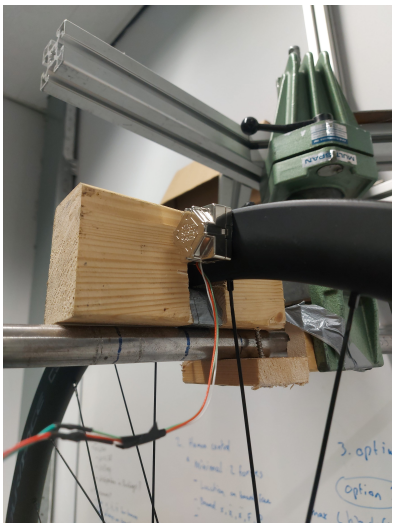

Figure 3.3: On the left, an image of the experimental set-up can be seen. The rim is freely suspended in a wooden block to prevent motion in other directions than the cycling direction. The angular speed sensor is attached close to the rotation point, on the rim. On the right, a close up of the sensor and the wooden block can be seen.

3.4 Curve fitting

The measured data from the experiments is fitted to the following equation:

$$Ae^{(-\lambda t)}cos\left((\omega^2 - \lambda^2)t + \phi\right) \tag{3.8}$$

Where A is the amplitude of the oscillations, λ is the decay rate, t is time, ω is the natural angular frequency of the oscillation and ϕ is the phase shift of the oscillation. An example of one of the fits to the measured oscillations of the bicycle wheels can be seen in Figure 3.4

3.5 Results

For every tire-rim combination, 3 measurements are done. In order to get an uncertainty on the precision of the angular frequency, the standard deviation of the mean angular frequency is taken on the 3 measurements. Using this information and Formula 3.7, the inertia of the measured wheel and the uncertainties are determined. The results of this can be seen in Figure 3.5 and Table 3.4. Bar graphs of the inertia for each tire width can be seen in Appendix A, A.2, A.3 and A.4.

In these figures, some error bars are larger than others. This is mainly due to the fact that not every wheel-tire combination is measured explicitly. Instead, some are combinations of measured combinations, increasing the uncertainty for these cases. Table 3.4 shows the inertia for all possible wheel-tire combinations.

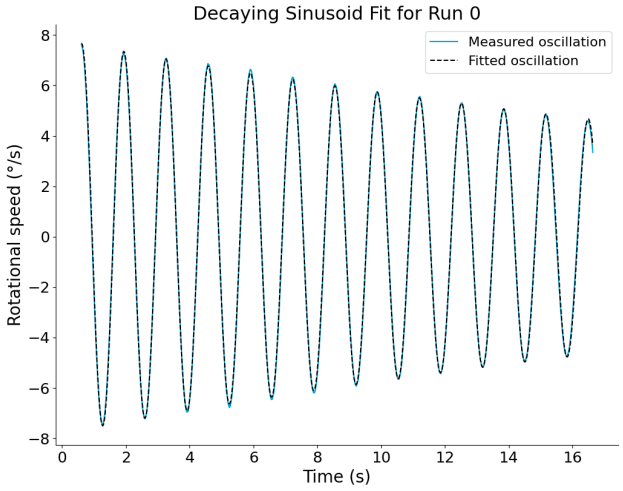

Figure 3.4: In this image, the fit of the decaying sinusoid on the measured data can be seen. The measured data in depicted in blue and the fit can be seen in black. It can be seen that the fit follows the measured data.

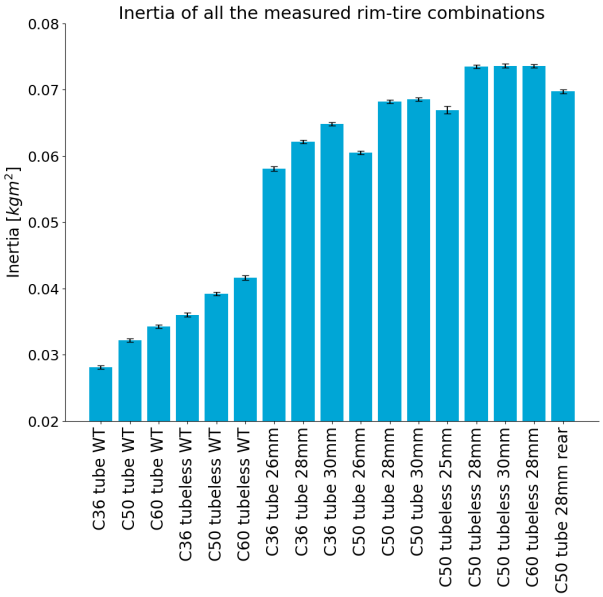

Figure 3.5: In this graph, all the different inertias of measured combinations can be seen. From these results, separate values for the different tires and rims can be constructed. "WT" stands for "Without tire".The measurements without tire are added to this graph so it can also be seen what the stake of the rim is in the total inertia of the wheel-tire combinations.

	Tube Inertia ($kg\,m^2$)		Tubeless Inertia ($kg\,m^2$)	
	C36 Front	C36 Rear	C36 Front	C36 Rear
Tire 26mm	$0.0573 \pm 3.50{\cdot}10^{-4}$	$0.0598 \pm 3.60{\cdot}10^{-4}$	$0.0636 \pm 6.19{\cdot}10^{-4}$	$0.0663 \pm 6.30{\cdot}10^{-4}$
Tire 28mm	$0.0632 \pm 2.78{\cdot}10^{-4}$	$0.0657 \pm 2.89{\cdot}10^{-4}$	$0.0692 \pm 3.81{\cdot}10^{-4}$	$0.0717 \pm 3.91{\cdot}10^{-4}$
Tire 30mm	$0.0647 \pm 2.83{\cdot}10^{-4}$	$0.0672 \pm 2.93{\cdot}10^{-4}$	$0.0704 \pm 4.06{\cdot}10^{-4}$	$0.0729 \pm 4.17{\cdot}10^{-4}$

	Tube Inertia ($kg\,m^2$)		Tubeless Inertia ($kg\,m^2$)	
	C50 Front	C50 Rear	C50 Front	C50 Rear
Tire 26mm	$0.0613 \pm 2.62{\cdot}10^{-4}$	$0.0638 \pm 2.72{\cdot}10^{-4}$	$0.0670 \pm 5.58{\cdot}10^{-4}$	$0.0695 \pm 5.68{\cdot}10^{-4}$
Tire 28mm	$0.0672 \pm 2.68{\cdot}10^{-4}$	$0.0697 \pm 2.79{\cdot}10^{-4}$	$0.0724 \pm 2.76{\cdot}10^{-4}$	$0.0749 \pm 2.87{\cdot}10^{-4}$
Tire 30mm	$0.0690 \pm 2.70{\cdot}10^{-4}$	$0.0712 \pm 2.81{\cdot}10^{-4}$	$0.0736 \pm 3.05{\cdot}10^{-4}$	$0.0761 \pm 3.16{\cdot}10^{-4}$

	Tube Inertia ($kg\,m^2$)		Tubeless Inertia ($kg\,m^2$)	
	C60 Front	C60 Rear	C60 Front	C60 Rear
Tire 26mm	$0.0634 \pm 3.89{\cdot}10^{-4}$	$0.0659 \pm 3.99{\cdot}10^{-4}$	$0.0693 \pm 6.59{\cdot}10^{-4}$	$0.0718 \pm 6.69{\cdot}10^{-4}$
Tire 28mm	$0.0693 \pm 3.63{\cdot}10^{-4}$	$0.0718 \pm 3.73{\cdot}10^{-4}$	$0.0747 \pm 2.66{\cdot}10^{-4}$	$0.0772 \pm 2.76{\cdot}10^{-4}$
Tire 30mm	$0.0708 \pm 3.66{\cdot}10^{-4}$	$0.0733 \pm 3.77{\cdot}10^{-4}$	$0.0760 \pm 4.64{\cdot}10^{-4}$	$0.0785 \pm 4.75{\cdot}10^{-4}$

Table 3.4: This table shows the rotational inertia for each of the wheel-tire sets available to Team DSM. All inertia are depicted in $kg\,m^2$. The uncertainty shown is one standard deviation, calculated from the measurement results.

4. Numerical Methods

In order to apply the equations in Chapter 2 to calculate the wind and simulate the cyclist, a numerical simulation is used. In this chapter, each step of this numerical simulation is explained. To do this, the structure of the flow chart in Figure 4.1 is used. In this figure, numbered processes can be seen. The dashed boxes in the figure represent inputs and the solid black boxes represent processes. In process 1, the latitude, longitude and speed for each cyclist for each moment in time in a race, is used to identify where turns are located in the race, in order to start process 2. In process 2, this turn identification is used to determine a braking force which is applied before a turn. It is assumed that braking only happens in a turn or right before a turn. In process 3, the non-linear equation presented as Equation 2.10 is solved to attain the wind speed. In process 4, using this wind speed and the original parameters, the point mass mentioned in Chapter 2 is forward simulated to obtain the original race time for the simulation, from now on referenced to as "Simulated Original Race Time". The Simulated Original Race Time needs to be determined since this is the baseline for the comparison for race times where other components are used. To clarify, the Simulated Original Race Time will be slightly different from the time that the physical cyclist took to complete the race. This time that the physical cyclist took to complete the race is from now on referenced to as the "Physical Race Time". Why there is a difference between the Simulated Original Race Time and the Physical Race Time, is explained in Chapter 5. In process 5, this same simulation is done with different values for m, I, C_DA and C_{rr}, from now on referenced to as "Simulated Race Times". These different values correspond to other wheel-tire combinations. In process 6, the Simulated Original Race Time is subtracted from the Simulated Race Times found for different wheel-tire combinations to produce the difference in race time for each wheel-tire combination, with respect to the Simulated Original Race Time. This difference in race time is from now on referenced to as "Race-Time Difference". This Race-Time Difference is then used to give advice on which wheel-tire combination to use. In this chapter, each of the processes in the flowchart is explained in detail.

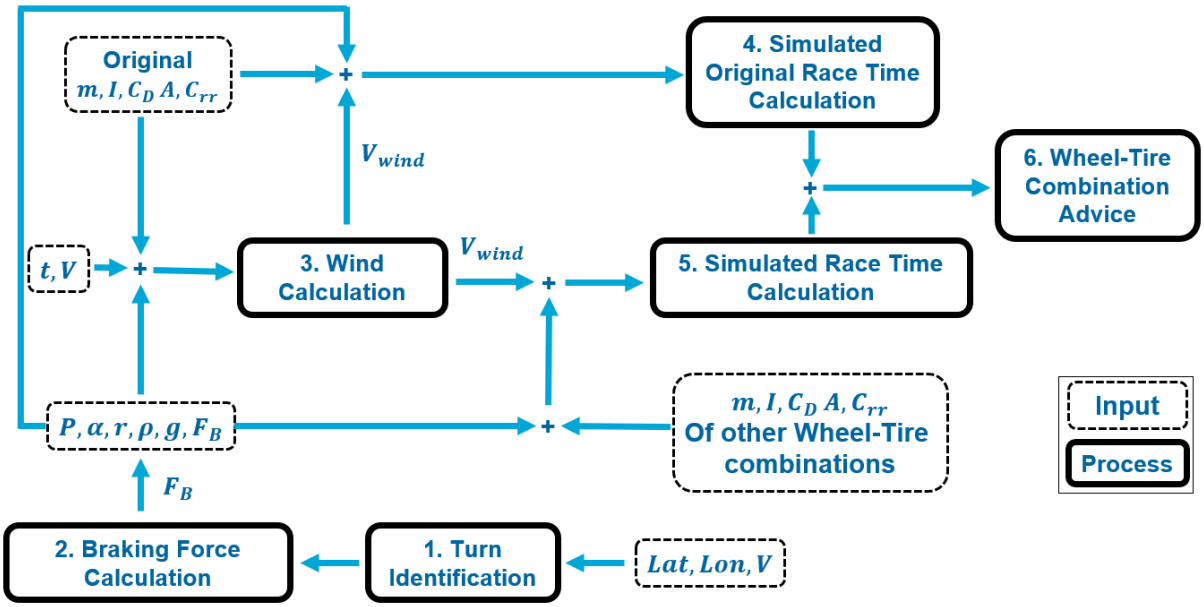

Figure 4.1: Flowchart of the numerical simulations done in this thesis. Each dashed box represents inputs and each solid black box represents a process. This flowchart shows 6 different processes. The processes are numbered to show in which order they are executed. The "+" shown in the figure, depict a combining of inputs. All the arrows approaching the plus are parameters, date or other results that are being grouped to be fed into the next process block.

4.1 Parameters

Each race as a specific elevation gain and length, which can be seen in Table 4.1. Here, the races "Brugge de Panne 2022" (Brugge), "Volta Ciclista Catalunya Stage 4 2022" (Catalunya), "Paris-Nice Stage 2 2022" (Paris) and "Volta a la Comunitat Valencia Stage 1 2022" (Valencia) are shown. Brugge and Paris are considered "flat" races. Catalunya and Valencia are considered "mountainous" races. The data sets for these races contain 6, 2, 6 and 3 cyclists, respectively. While using different wheel-tire combinations for Catalunya and Valencia, it was sometimes encountered that a cyclist would not have enough power available in the power data, to pass over certain hills. Those cyclists are omitted from this research. This concerns 2 cyclists in both Catalunya and Valencia.

Race	Length (km)	Accumulated elevation gain (m)
Brugge de Panne 2022	205.9	418
Volta Ciclista Catalunya Stage 4 2022	167.1	3420
Paris-Nice Stage 2 2022	159.2	895
Volta a la Comunitat Valencia Stage 1 2022	166.5	3130

Table 4.1: Table that shows the length and the elevation gain for the races that were analysed in this Thesis

These races are chosen because they differ greatly in elevation gain and Team DSM has chosen different components among these races. Since this study uses data from races that have already been raced, component choices have already been made for these races. The relevant components that were used for these races can be seen in Table 4.2.

Race	Rim type	Tire width
Brugge	C60 Tubular	26mm
Catalunya	C36 Tubular	26mm
Paris-Nice Stage 2 2022	C60 Tubular	26mm
Volta a la Comunitat Valencia Stage 1 2022	C36 Tubular	26mm

Table 4.2: Component choices that Team DSM made for the races that are analysed in this Thesis

The differences in mass and inertia for the different wheels and tires can be found in Chapter 3 (Table 3.2 & 3.4). The rolling resistance coefficient for different tires can be seen in Table 4.3. It can be seen that the rolling resistance of tubeless tires is smaller than that of tubular tires. It can also be seen that the rolling resistance of a wider tire is higher than the rolling resistance for a narrower tire.

	26mm Tubular	26mm Tubeless	28mm Tubular	28mm Tubeless
C_{rr}	0.00198	0.001522	0.002547	0.002089

Table 4.3: The coefficient of rolling resistance for tubular tires and tubeless tires for different sizes. The rolling resistance for tubeless tires is smaller than that of tubular tires.

The differences in C_DA for wheel-tire combinations are explained in the next subsection (4.1.1). All other parameters, like the mass of the cyclist, gravitational constant, air density etc. stay consistent for each step in the flow chart, for each individual cyclist. These parameters can be found in Appendix B, Tables B.3, B.4 and B.5.

4.1.1 Aerodynamic drag coefficient

The C_DA for the cyclist and their bicycle is determined as follows: First, a "base C_DA" is loaded. This is a C_DA from the measurements that Team DSM performed on time-trial bicycles. Then, depending on the slope of the road, this base C_DA is multiplied by 1.15 if the slope is less than -6.5%, by 1.65 if the slope is larger than 5% and by 1.35 if the slope is in between these 2 values. These values were suggested by Team DSM. This represents the influence of posture on the C_DA of the cyclist when descending or ascending. The C_DA of a cyclist on a road bicycle is larger than the C_DA of a cyclist on a time-trial bicycle.

Different rims have different air resistances, which is captured in the value of the C_DA. Team DSM has supplied a report, in which they analyzed how many seconds a cyclist in a time-trial spends in different (absolute) yaw-angle ranges. Team DSM also conducted wind tunnel tests that show the difference in C_DA for each wheel-tire combination, at different yaw-angles. Combining these wind tunnel test with the yaw angle analysis, a C_DA difference between wheels can be approximated. This results in the C_DA differences that can be seen in Table 4.4. The C_DA difference for tubular and tubeless wheels is assumed to be equal. Details of this C_DA difference calculation can be found in Appendix B, Table B.6 and B.7. These differences are added to the value of the C_DA after the multiplication that accounts for the posture, to account for the wheel choice.

	C36 26mm	C36 28mm	C50 26mm	C50 28mm	C60 26mm	C60 28mm
C_DA difference	0.00088601	0.00107879	0	0.0001462	-0.00069772	-0.000193

Table 4.4: Table in which the C_DA differences between the 3 different rim-types can be seen. It is assumed that tubeless and tubular rims have the same aerodynamic properties

4.2 Braking force

Since it is assumed that the braking force is only applied in turns, it is important to identify where turns are. Step 1 in the flow chart does this. In order to do this, 3 different type of turns are defined, namely an "easy turn" (30-40°), a "medium turn" (40-70°) and a "sharp turn" (70+°). Using these definitions, the average speed in these types of turns is determined and uses as "ΔV" in the Braking Force Equation 2.8.

4.2.1 Turn Identification

First, the locations where the braking force should be applied are defined. To determine this, the latitude and longitude coordinates from the race data are transformed to X-Y coordinates using the Universal Transverse Mercator (UTM) projection. This projection converts spherical coordinates to rectangular coordinates. This projection has a scale error, which is usually smaller than 0.1% [36]. To do this, the Python package "utm" is used [37]. This package automatically picks the best-suited UTM projection based on the latitude and longitude it receives. Using this projection, 2 vectors from 4 points (point A, B, C & D) are created for all the points in the race course. Point A and B are 2 consecutive points and point C and D are as well. Between point B and point C, a space of 100m is left. This can be seen in Figure 4.2 as well. Then, for each turn-type, a iteration of all points is done, moving A, B, C and D through the course. For each step, the heading difference between the vector $\vec{AB}$ and vector $\vec{CD}$ is

calculated using the properties of the internal product (Equation 4.1). Each time a turn is found, the distance between B and C is skipped, to prevent identifying the same turn multiple times.

$$\alpha = cos^{-1}\left(\frac{\vec{AB} \cdot \vec{CD}}{|\vec{AB}||\vec{CD}|}\right) \tag{4.1}$$

The first iteration looks for the easy turns. For every easy turn found, the turn is saved and mapped to a distance in the race. The second iteration looks for the medium turns. For every medium turn found, the turn is saved and mapped to a distance in the race as well. However, if the same location is found for a medium turn as for an easy turn, the easy turn is overwritten. The same iteration as for the medium turns is executed for the sharp turns. In this case, a sharp turn would overwrite the medium turn and the easy turn.

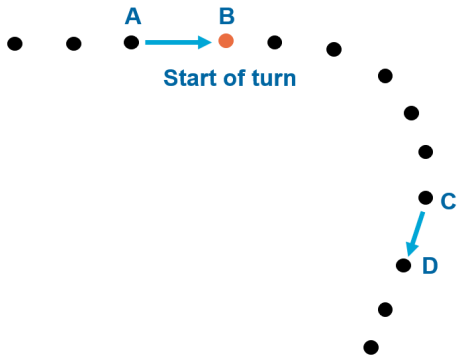

Figure 4.2: Figure that shows an abstract image of the turn identification for the braking force.

4.2.2 Braking force calculation

Now, the easy, medium and sharp turns are defined and mapped to locations along the race course. For each of these turns classifications, the average speed is calculated and this can be seen in Table 4.5. This turning average speed is used to determine the braking force for the cyclist as can be seen in Equation 2.8. Here, ΔV is the difference between the current speed of the cyclist and the average turn speed, for that turn identification. A sample of the locations of the turns, the speed for each individual turn and the cycling direction can be seen in Figure 4.3.

Race	Speed (m/s)			
	Average	Easy turn	Medium turn	Sharp turn
Brugge	11.8	9.6	8.7	6.9
Catalunya	9.8	9.5	8.9	6.5
Paris	12.8	10.9	9.2	6.0
Valencia	10.4	9.8	9.6	6.0

Table 4.5: Table that shows the average speeds in the selected turn identification. It can be seen that all the average cornering speeds are lower than the average cycling speed. A sharper turn identification also results in a slower average speed compared to an easier turn.

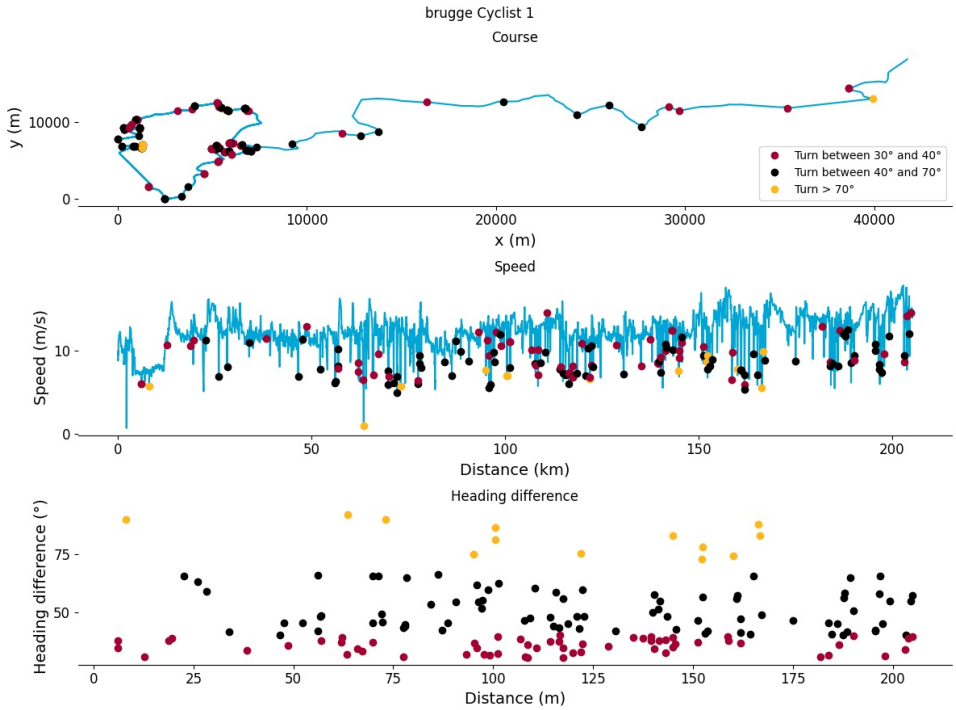

Figure 4.3: Figure which shows the result of a turn-identification. The turns that are identified are plotted on the course in the top plot. The colors of the identified turns indicate whether a turn was identified as easy, medium or sharp. The same turns are also plotted on the speed over distance, to show what the speed has been during a turn. Lastly, the lower plot shows the angle at which the turn was identified.

4.3 Wind Calculation

To attain the wind speed experienced by the cyclist, the non-linear Equation 2.10 is solved for V_{wind}, using the Python package "scipy.optimize.fsolve" (fsolve) [33]. This Python package finds the roots of a (non)linear equation. Equation 2.10 has 3 roots. In order to pick a solution, an estimation for V_{wind} is given to fsolve. This estimation is set as being Equation 2.12, which is time dependent on power, speed and slope. The derivation for Equation 2.12 is given in Chapter 2. When solving for V_{wind}, it can be seen in Figure 4.1 what the input parameters for this are. Important to know is that V, P, and α are time-dependent. Due to this time-dependency, the solution for V_{wind} is also time-dependent. To calculate the acceleration, the Python package "derivative 0.4.2" is used [38]. In this Python package, the central difference method is used to calculate the acceleration from the speed data. Here, the derivative of $f(t)$ is calculated using Equation 4.2.

$$f'(t) = \frac{f(t+h) - f(t-h)}{2h} \tag{4.2}$$

Where $f(t)$ is the velocity and $f'(t)$ is the approximated acceleration of the cyclist. h is the time step between the current, next and previous point in the data-set. In this case, h is determined by the sample frequency of the bicycle computer used by Team DSM, which is $1Hz$. The method used to calculate the wind speed is validated in Appendix B.3.1

4.3.1 Output

When the necessary parameters are fed into step 3 in the flow chart, the wind is calculated. A sample of the solution for the wind speed can be seen in Figure 4.4. These samples of the time series for the wind speed show a greatly variable wind. This variability of these sample is indicative for what the rest of the time series looks like.

The average wind speeds for each cyclist for each different race can be seen in Table 4.6. In this table, it can be seen that the average wind speeds are consistently smaller than 0. This would mean that on average, the cyclist "experienced" a tailwind. In these races, cyclists cycle in different wind directions,

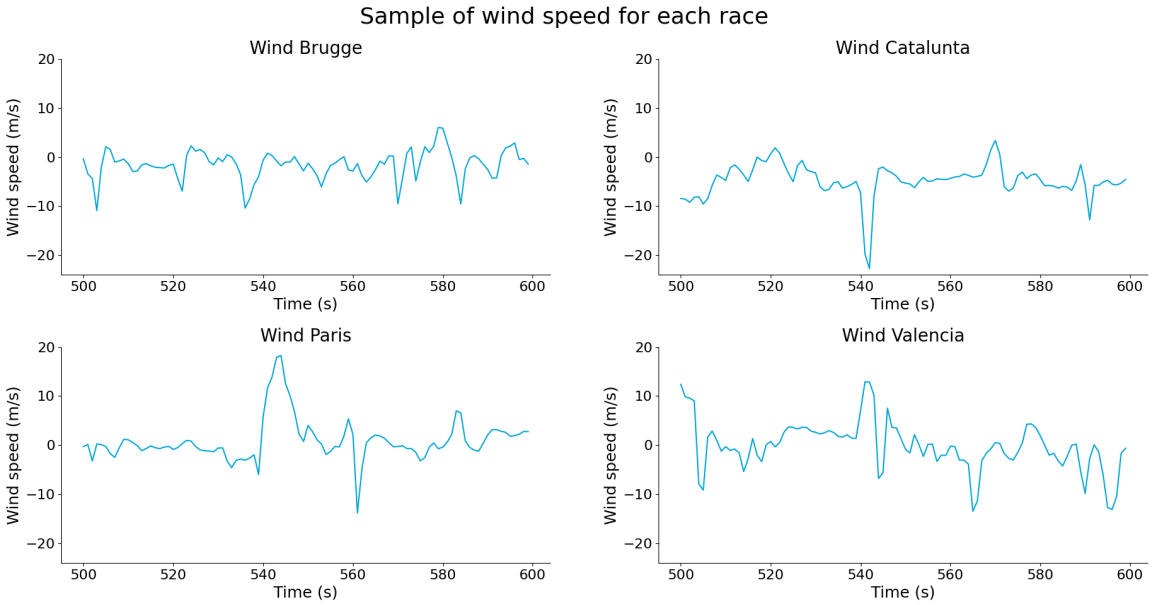

Figure 4.4: Figure that shows a sample of 100s of the solution for the wind speed for each race. It can be seen that the wind speed is greatly variable over time and has large peaks and valleys. This indicative of how the complete time series looks

if not all wind directions. If there were to be a north wind on that day, if cyclists cycle both to the north and to the south, one would expect to see a tailwind and a headwind. It is unlikely that the wind shifted during these races to be a constant tailwind for these cyclists. The reason that the wind speeds are consistently smaller than 0, is because the "wind speed" that is calculated captures the drag reduction from drafting. Imagine cycling in an environment without wind. In this environment, it is still beneficial to draft behind other cyclists. This is because of the low-pressure area in the wake of the other cyclist. This negative average wind speed effectively enables this drag reduction, by reducing the drag force (see Equation 2.3). So if a cyclist would draft in an environment without wind, the "wind speed" would show as a tailwind. These "wind speeds" are bounded by the power and speeds data from the cyclist. A cyclist can only overcome a limited aerodynamic drag with the power delivered at each time instance. The magnitude of the wind speed is determined by how much power is put in by the cyclist and how fast the cyclist is going, according to the data received from Team DSM.

	Brugge	Catalunya	Paris	Valencia
Cyclist 1	-3.57m/s	-2.02 m/s	-3.30m/s	-2.24m/s
Cyclist 2	-3.66m/s	-1.58 m/s	-2.60m/s	-3.08m/s
Cyclist 3	-4.01m/s	- m/s	-3.82m/s	-3.24m/s
Cyclist 4	-4.20m/s	- m/s	-3.30m/s	- m/s
Cyclist 5	-4.01m/s	- m/s	-3.92m/s	- m/s
Cyclist 6	-3.41m/s	- m/s	-2.96m/s	- m/s

Table 4.6: Table that shows the average wind speed for each cyclist in each race. It can be seen that the average wind speeds are consistently smaller than 0.

4.4 Original race-time calculation

As can be seen in the flow chart, the next step is to calculate the Simulated Original Race Time. This is acquired by forward simulating the cyclist with the original wheel-tire setup. Due to interpolation methods, truncation errors, central differencing method and the wind solution, the Physical Race Time and the Simulated Original Race Time are going to differ. More about this error is explained in Chapter 5, section 5.2. The Simulated Original Race Time is calculated to have a benchmark to compare the Simulated Race Times to.

4.4.1 Integration

In order to simulate the cyclist over the race course, the Python package scipy.integrate.solve_ivp (solve_ivp) is used [33]. This package numerically integrates a system of Ordinary Differential Equations (ODEs). For each iteration, the current speed and distance, along with the rest of the forces acting on the cyclist, are passed to solve_ivp. Solve_ivp numerically integrates this input to attain a new speed and distance by differentiating the current speed and distance with respect to time. To do this, the integration method and tolerances need to be chosen. As integration method, "DOP853" is used. DOP853 is an eighth-order explicit Runge-Kutta method. An explicit integration method calculates the future state of the system, using the current state of the system. An implicit method calculates the future state from the system state at present and future times. An explicit integration method is generally faster per step but needs a smaller step size in order to remain stable. An implicit method can use larger step sizes while still remaining stable. Every step in an implicit method is generally slower.

When using an integration function with a variable time step like solve_ivp, the tolerances are guiding for the size of the time step used. An estimation for the result of each step is made for the desired order and one order below. In this case, this is an eighth-order and a seventh-order solution. Assume that the result of the eighth-order solution is called y_{n+1}, with an error of order $O((\Delta t)^9)$. Assume that the result of the seventh order solution is called Y_{n+1}, with an error of order $O((\Delta t)^8)$. From this, the "actual error" (e) can be defined, see Equation 4.3. This actual error will contain an error of order $O((\Delta t)^8)$ [39].

$$e = |y_{n+1} - Y_{n+1}| \tag{4.3}$$

The "allowed error" (ϵ) is defined by the user, setting the tolerances for the integration (see Equation 4.4). Where $atol$ is the absolute tolerance and $rtol$ is the relative tolerance. The absolute tolerance is defined as: $|e| <= atol$ and the relative tolerance is defined as $|e| <= rtol \cdot |Y_{n+1}|$.

$$\epsilon = atol + rtol|y| \tag{4.4}$$

Solve_ivp keeps the actual error smaller than the allowed error by changing the time step for the integration according to Equation 4.5.

$$\Delta\tau = \Delta t \left(\frac{\epsilon}{e}\right)^{\frac{1}{8}} \tag{4.5}$$

Here, $\Delta\tau$ is the time step necessary to stay within the error margins. Δt is the time step that was used to obtain both y_{n+1} and Y_{n+1}. This poses 3 scenarios:

1. $e > \epsilon$, in which case the solution is rejected and Δt is reduced to $\Delta\tau$ to obtain a more accurate solution.
2. $e < \epsilon$, in which case the solution is accepted and Δt can be increased to achieve faster integration.
3. $e = \epsilon$, in which case the solution is accepted

This means that higher tolerances give a more accurate solution. It will take more time to integrate since it will take more iterations due to the smaller time-steps. The tolerances chosen for this purpose are $rtol = 1e-12$ and $atol = 1e-12$. The reasoning behind this choice is further explained in Chapter 5.

4.4.2 Interpolation

During the integration by solve_ivp, the power, wind speed and slope need to be available as a function of distance. The initial data from Team DSM has a sampling rate of $1Hz$. Interpolation functions are created to be able to access power, wind speed and slope on each requested distance. To do this, the Python package scipy.interpolate.interp1d is used [33]. This function maps the power, wind speed and slope to distance. As interpolation method, first order interpolation is chosen.

4.5 Race time calculation different wheel-tire combinations

When calculating the Simulated Race Times for different wheel-tire combinations, the same process is used as for the Simulated Original Race Time calculation. However, in this iteration of the process, the mass, inertia, C_DA and C_{rr} of the original components are replaced by the values for different wheel-tire combinations. For each of these combinations, the simulation is run and the Simulated Race Time for each combination is calculated. These results can then be compared to the Simulated Original Race Time in step 6 of the flow chart.

4.6 Wheel-tire combination advice

Combining step 4 and 5 from the flow chart, the Simulated Race Time for each wheel-tire combination and the Simulated Original Race Time are attained. Now, the Simulated Original Race Time can be subtracted from the Simulated Race Time to produce the Race Time Difference. When the Simulated Race Time is longer than the Simulated Original Race Time for a different wheel-tire combination, this means that the wheel-tire combination is slower than the original set-up. When the race time is smaller than the original race time, the opposite is true. All individual race times can be compared as well, to determine not only which wheel-tire combinations would have been faster than the original wheel-tire combinations but also which wheel-tire combination is fastest overall.

5. Error Estimation

In order to evaluate the influence of the error in the measurements of the parameters and the simulation on the result, the following steps are taken. First, the uncertainty of the parameters used in the simulation is analyzed. After that, the difference in the Simulated Original Race Time and the Physical Time is shown. Finally, a sensitivity analysis is performed for the different parameters in the simulation. This sensitivity analysis is only performed for 1 cyclist in each race (Cyclist 2). Using this sensitivity analysis, the uncertainty on the Simulated Race Times for the different wheel-tire combinations is shown. The tolerances for the numerical integration that produces the Simulated Race Times are discussed. All numerical integration for error estimation is done using the Python package scipy.integrate.solve_ivp, using integration method "DOP853". The tolerances used are $rtol = 1e^{-12}$ and $atol = 1e^{-12}$ [33, 40], unless otherwise mentioned.

5.1 Parameters

Looking at table 5.1, it can be seen that only the uncertainty on the coefficient of drag, the inertia and the mass of the wheels is known. It is assumed that there is no uncertainty on the gravitational constant and the density of the air. The mass of the cyclist is measured individually by each cyclist on different scales. The slope, power and speed are dependent on the measurement accuracy of the bicycle computer used by Team DSM, which is unknown. The bicycle computer that is used, is the "Wahoo ELEMNT BOLT". The measurements on the coefficient of rolling resistance, received from Team DSM, are not elaborate enough to be able to determine a standard deviation. The uncertainties in both CdA and I are in a confidence interval of 95.4%. The uncertainty on the mass of the wheels represents the measurement resolution of the scale used. When comparing different wheel-tire combinations, the same power, slope, speed, gravitational constant, air density, cyclist mass and wheel-radius are used. This makes the error on these parameters less relevant than the error on the coefficient of rolling resistance, coefficient of drag, rotational inertia and mass of the wheels.

Unknown uncertainty	Known uncertainty	Uncertainty
g	C_DA (bicycle)	± 0.00042
ρ	I (wheel)	See Table 3.4
m cyclist	m (wheel)	$\pm 0.5g$
C_DA (cyclist)		
Slope		
Power		
V		
r		
C_{rr}		

Table 5.1: Table that shows for which parameters the uncertainty is unknown and for which parameters the uncertainty is known. For parameters with a known uncertainty, the uncertainty is given. For C_DA and I, the uncertainty is within a 95.4% confidence interval. For m, the uncertainty represents the measurement accuracy of the scale used.

5.2 Race Time accuracy

In Table 5.2, the Physical Race Times, Simulated Original Race Times without braking and the Simulated Race Times can be seen. To obtain Simulated Original Race Times without braking, a wind speed is calculated without a braking force. Using this wind speed, Simulated Original Race Time without braking is calculated. To obtain the regular Simulated Original Race time, braking is always used throughout this entire thesis. This means that the calculation for the Simulated Original Race Time is done with

braking enabled for both the wind speed calculation and the race time calculation. The difference the Physical Race Time and the Original Race Time without braking that can be seen in Table 5.2 is due to interpolation, truncation errors, central differencing method and the wind solution. Especially the numerical derivative (as mentioned in Chapter 4) could cause this difference in race time between the real race and the simulated race. Wind speed, slope, and power are interpolated during the Simulated Original Race Time calculation and the Simulated Race Time calculation. For interpolation, the Python package "scipy.interpolate.interp1d" is used, using a first-order interpolation. The wind solution has cases where the solution wants to go to negative infinity or positive infinity. In these cases, the wind solution is set at $-V$. The frequency with which this happens can be seen in Appendix B, Table B.8.

There is also a difference in the race time between the Simulated Original Race Time without braking and the Simulated Original Race Time. This is caused by the difference in step size used for the wind calculation and the race time calculation. Due to the step size of the numerical integration, small parts of the braking window are missed in the numerical integration, which causes the Simulated Original Race Time to be slightly faster than the Simulated Original Race Time without braking. Any other Simulated Race Time or Simulated Original Race Time in this thesis is calculated using braking.

Race	Physical Race Time	Simulated Original Race Time without Braking	Simulated Original Race Time
Brugge (1)	$17155s$	$17107s$	$17102s$
Catalunya (1)	$16696s$	$16544s$	$16537s$
Paris (1)	$12342s$	$12513s$	$12511s$
Valencia (1)	$15944s$	$16106s$	$16097s$

Table 5.2: Table which shows the Physical Race Time, The Simulated Original Race Time without braking and the Simulated Original Race Time.

5.3 Sensitivity analysis

A sensitivity analysis is performed for the parameters used in each race. The results of this analysis can be seen in Table 5.3. This analysis is done by increasing the value of the parameters with 1%, 2% and 3% when calculating the Simulated Original Race Time. Using the definition of a partial derivative, as can be seen in Equation 5.1, the change in Simulated Original Race Time for each parameter is quantified. Here, $f'(a)$ is the partial derivative of the Simulated Original Race Time with respect to a change in parameter a. $f(a)$ is the Simulated Original Race Time value for the unchanged parameter, $f(a+h)$ is the Simulated Original Race Time value for the parameter with the increase of h when h is the change in the parameter. In this table, it can be seen that mass is more important for the mountainous stages than for the flatter stages. It can also be seen that increasing the rotational inertia, decreases the Simulated Original Race Time, which is unexpected. This is because the amount of braking that occurs during a race and the magnitude of the braking force is underestimated in this model. When the braking is artificially increased, the sensitivity of the Simulated Original Race Time to the rotational inertia changes to be positive instead of negative. The wind speed adds energy to the system in some cases. When this energy is not dissipated in some way, it can cause the inertia sensitivity to be negative. This leads to the conclusion that the braking protocol should be revised in the future. In the section "Result Estimation" of this chapter, the effects of this fault on the inertia sensitivity are shown.

$$f'_a(a) = \frac{f(a+h) - f(a)}{h} \tag{5.1}$$

In Table 5.4, the sensitivity for parameters per $10km$ can be seen. Where aerodynamics are usually suspected to have a larger impact on cycling performance than rolling resistance, it can be seen that a small change in value for C_{rr} can cause large changes in this model. Generally, the values for $C_D A$ are 100 times larger than the values for C_{rr}. This is why these values become more intuitive to interpret when put into perspective of a realistic change in parameter. This is done in Section 5.5, where this sensitivity is used to create a better understanding of the actual impact of a realistic change in these values.

Parameter	Brugge	Catalunya	Paris	Valencia
$m\ (s/kg)$	2.5	40.3	3.3	32.7
$I\ (s/(kg\,m^2))$	-14.1	-19.2	-34.9	-4.9
$C_DA\ (s/1)$	23927.0	18134.0	18763.7	20080.5
$C_{rr}\ (s/1)$	260164.9	190227.8	159891.1	190161.4
$P\ (s/W)$	-24.4	-29.8	-13.4	-30.5
$V_{wind}\ (s/(m/s))$	798.8	699.1	657.3	727.4

Table 5.3: Table that shows the average of the results for the sensitivity analysis of the four different races.

Parameter	Brugge	Catalunya	Paris	Valencia
$m\ ((s/kg)/10km)$	0.1	2.5	0.2	2.0
$I\ ((s/(kg\,m^2))/10km)$	-0.7	-1.2	-2.2	-0.29
$C_DA\ ((s/1)/10km)$	1165.8	1103.3	1180.3	1210.1
$C_{rr}\ ((s/1)/10km)$	12676.2	11574.2	10057.5	11459.2
$P\ ((s/W)/10km)$	-1.2	-1.8	-0.8	-1.8
$V_{wind}\ ((s/(m/s))/10km)$	38.5	42.5	41.3	43.8

Table 5.4: Table that shows the results of the sensitivity analysis for the four different races, scaled to represent a time change per 10km, per change of parameter value.

5.4 Error estimation due to error in parameters

In Table 5.5, the sensitivity analysis is used to approximate the error in Simulated Original Race Time and the Simulated Race Time for each parameter of which the uncertainty is known. These errors are then added to present a total uncertainty in the simulations. The values in this table are obtained by multiplying the uncertainty of the parameter by the sensitivity of that parameter for each race. In this, it can be seen that the uncertainties on inertia and mass are relatively small compared to the uncertainties on aerodynamics. The C_{rr} is missing from the table, as no estimation of the uncertainty could be made for this parameter.

Brugge 26mm	C36	C50	C60	C36TL	C50TL	C60TL
m (wheel)	$\pm 3.5 \cdot 10^{-3} s$	$\pm 3.5 \cdot 10^{-3} s$	$\pm 3.5 \cdot 10^{-3} s$	$\pm 3.5 \cdot 10^{-3} s$	$\pm 3.5 \cdot 10^{-3} s$	$\pm 3.5 \cdot 10^{-3} s$
I	$\pm 1.4 \cdot 10^{-2} s$	$\pm 1.1 \cdot 10^{-2} s$	$\pm 1.6 \cdot 10^{-3} s$	$\pm 2.5 \cdot 10^{-2} s$	$\pm 2.3 \cdot 10^{-2} s$	$\pm 2.6 \cdot 10^{-2} s$
$C_D A$	$\pm 10.0 s$	$\pm 10.0 s$	$\pm 10.0 s$	$\pm 10.0 s$	$\pm 10.0 s$	$\pm 10.0 s$
Total	$\pm 10.067 s$	$\pm 10.063 s$	$\pm 10.069 s$	$\pm 10.078 s$	$\pm 10.075 s$	$\pm 10.079 s$

Catalunya 26mm	C36	C50	C60	C36TL	C50TL	C60TL
m (wheel)	$\pm 5.6 \cdot 10^{-2} s$	$\pm 5.6 \cdot 10^{-2} s$	$\pm 5.6 \cdot 10^{-2} s$	$\pm 5.6 \cdot 10^{-2} s$	$\pm 5.6 \cdot 10^{-2} s$	$\pm 5.6 \cdot 10^{-2} s$
I	$\pm 1.9 \cdot 10^{-2} s$	$\pm 1.5 \cdot 10^{-2} s$	$\pm 2.1 \cdot 10^{-2} s$	$\pm 3.4 \cdot 10^{-2} s$	$\pm 3.1 \cdot 10^{-2} s$	$\pm 3.6 \cdot 10^{-2} s$
$C_D A$	$\pm 7.6 s$	$\pm 7.6 s$	$\pm 7.6 s$	$\pm 7.6 s$	$\pm 7.6 s$	$\pm 7.6 s$
Total	± 7.6915	$\pm 7.6867 s$	$\pm 7.6937 s$	$\pm 7.7069 s$	$\pm 7.7029 s$	$\pm 7.7083 s$

Paris 26mm	C36	C50	C60	C36TL	C50TL	C60TL
m (wheel)	$\pm 4.7 \cdot 10^{-3} s$	$\pm 4.7 \cdot 10^{-3} s$	$\pm 4.7 \cdot 10^{-3} s$	$\pm 4.7 \cdot 10^{-3} s$	$\pm 4.7 \cdot 10^{-3} s$	$\pm 4.7 \cdot 10^{-3} s$
I	$\pm 3.5 \cdot 10^{-2} s$	$\pm 2.6 \cdot 10^{-2} s$	$\pm 3.9 \cdot 10^{-2} s$	$\pm 6.2 \cdot 10^{-2} s$	$\pm 5.6 \cdot 10^{-2} s$	$\pm 6.6 \cdot 10^{-2} s$
$C_D A$	$\pm 7.9 s$	$\pm 7.9 s$	$\pm 7.9 s$	$\pm 7.9 s$	$\pm 7.9 s$	$\pm 7.9 s$
Total	± 7.9205	$\pm 7.9118 s$	$\pm 7.9243 s$	$\pm 7.9471 s$	$\pm 7.9410 s$	$\pm 7.9510 s$

Valencia 26mm	C36	C50	C60	C36TL	C50TL	C60TL
m (wheel)	$\pm 4.6 \cdot 10^{-2} s$	$\pm 4.6 \cdot 10^{-2} s$	$\pm 4.6 \cdot 10^{-2} s$	$\pm 4.6 \cdot 10^{-2} s$	$\pm 4.6 \cdot 10^{-2} s$	$\pm 4.6 \cdot 10^{-2} s$
I	$\pm 4.9 \cdot 10^{-3} s$	$\pm 3.7 \cdot 10^{-3} s$	$\pm 5.5 \cdot 10^{-3} s$	$\pm 8.7 \cdot 10^{-3} s$	$\pm 7.8 \cdot 10^{-3} s$	$\pm 9.2 \cdot 10^{-3} s$
$C_D A$	$\pm 8.4 s$	$\pm 8.4 s$	$\pm 8.4 s$	$\pm 8.4 s$	$\pm 8.4 s$	$\pm 8.4 s$
Total	± 8.4847	$\pm 8.4835 s$	$\pm 8.4853 s$	$\pm 8.4885 s$	$\pm 8.4876 s$	$\pm 8.4890 s$

Table 5.5: Table that shows the uncertainty for the mass of the wheel, inertia of the wheel and the $C_D A$ of the bicycle for Brugge, Catalunya, Paris and Valencia. Table also shows the total uncertainty over these 3 parameters together, for each race.

5.5 Result Estimation

In Table 5.6, the expected Race Time Differences for the change in wheel-tire combinations is shown, as predicted by the sensitivity analysis. The contribution in Race Time Difference for each parameter can be seen as well. These estimations are made by multiplying the difference in weight, rotational inertia, $C_D A$ and C_{rr} by the sensitivity of these parameters for each race. The estimated Race Time Difference is attained by adding the contributions in Race Time Difference for each parameter. This shows that changes in rolling resistance and aerodynamic drag between wheel-tire combinations have the largest effect. If the amount of braking is increased, the effect of rotational inertia will increase with it. However, it will have to increase a large amount before this will influence the decision of which wheel-tire combination is preferred. Since the aerodynamic uncertainty is large, it cannot be said with certainty that the C50 rim is faster than the C36. In those cases, the aerodynamic uncertainty would overlap. This is especially true for Catalunya and Valenica. However, the Race Time Difference estimation shows that between C36 and C60, no uncertainty overlap occurs. This would mean that the C60 is faster than the C36 for all of the races that were analyzed. C_{rr} has large effects on the results as well, showing that tubeless is faster than tubular. However, since no uncertainty is known on the C_{rr}, it cannot be said what the reliability of this result is.

Brugge 26mm	C36	C50	C60	C36TL	C50TL	C60TL
m	$-0.73s$	$-0.40s$	$0s$	$-0.31s$	$0.045s$	$0.43s$
I	$0.17s$	$0.06s$	$0s$	$-0.01s$	$-0.10s$	$-0.17s$
C_DA	$38.65s$	$18.60s$	$0s$	$38.65s$	$18.60s$	$0s$
C_{rr}	$0s$	$0s$	$0s$	$-119.15s$	$-119.15s$	$-119.15s$
Total	$38.09s$	$18.26s$	$0s$	$-80.83s$	$-100.61s$	$-118.89s$

Catalunya 26mm	C36	C50	C60	C36TL	C50TL	C60TL
m	$0s$	$5.32s$	$11.77s$	$6.77s$	$12.49s$	$18.70s$
I	$0s$	$-0.15s$	$-0.23s$	$-0.25s$	$-0.37s$	$-0.46s$
C_DA	$0s$	$-15.19s$	$-29.29s$	$0s$	$-15.19s$	$-29.29s$
C_{rr}	$0s$	$0s$	$0s$	$-87.12s$	$-87.12s$	$-87.12s$
Total	$0s$	$-10.03s$	$-17.76s$	$-80.60s$	$-90.20s$	$-98.18s$

Paris 26mm	C36	C50	C60	C36TL	C50TL	C60TL
m	$-0.96s$	$-0.53s$	$0s$	$-0.41s$	$0.06s$	$0.57s$
I	$0.43s$	$0.15s$	$0s$	$-0.02s$	$-0.25s$	$-0.41s$
C_DA	$30.3s$	$14.6s$	$0s$	$30.3s$	$14.6s$	$0s$
C_{rr}	$0s$	$0s$	$0s$	$-73.23s$	$-73.23s$	$-73.23s$
Total	$29.77s$	$14.20s$	$0s$	$-43.35s$	$-58.84s$	$-73.07s$

Valencia 26mm	C36	C50	C60	C36TL	C50TL	C60TL
m	$0s$	$5.32s$	$11.77s$	$6.77s$	$12.49s$	$18.70s$
I	$0s$	$-0.15s$	$-0.23s$	$-0.25s$	$-0.37s$	$-0.46s$
C_DA	$0s$	$-16.83s$	$-32.43s$	$0s$	$-16.83s$	$-32.43s$
C_{rr}	$0s$	$0s$	$0s$	$-87.09s$	$-87.09s$	$-87.09s$
Total	$0s$	$-12.55s$	$-22.95s$	$-81.66s$	$-93.88s$	$-104.47s$

Table 5.6: Table that shows the estimation of the expected Race Time Differences for different wheel-tire combinations, for Brugge, Catalunya, Paris and Valencia, based on the sensitivity of the model.

5.6 Numerical Integration

DOP853 is chosen as the integration scheme since it is a higher order method (eight order). Higher order method require fewer steps than lower order methods, decreasing the accumulation of round-off errors. Since the integration takes a few million steps, integrating over the race time, errors in the integration can accumulate. Higher order methods have a smaller overall error per step, which means that less error is accumulated over the entire process of the integration.

While choosing the tolerances for the numerical integration, a deviation of more than 30 seconds can be seen in the Simulated Original Race Time results, between the tightest and the loosest tolerances (Table 5.7).

	Brugge	Catalunya	Paris	Valencia
$rtol = 1e-3$, $atol = 1e-6$	$17082.0s$	$16503.9s$	$12509.3s$	$16075.8s$
$rtol = 1e-6$, $atol = 1e-8$	$17075.5s$	$16522.2s$	$12506.7s$	$16078.7s$
$rtol = 1e-8$, $atol = 1e-10$	$17076.7s$	$16521.4s$	$12505.9s$	$16079.8s$
$rtol = 1e-12$, $atol = 1e-12$	$17102.1s$	$16537.0s$	$12510.5s$	$16097.2s$

Table 5.7: Table that shows the Simulated Original Race Times for different tolerances using the DOP853 integration method with solve_ivp.

Looking at the Simulated Original Race Time results in Table 5.7, it can be seen that the race time generally converges to the race time found with the tightest tolerances when tightening the tolerances. The rate at which this happens is not fast enough in light of the uncertainty over C_DA. Since the uncertainty on C_DA is relatively high and the uncertainty on C_{rr} is unknown, it is chosen to run all simulations with tolerances $rtol = 1e-12$ and $atol = 1e-12$. This is done to reduce the error from the numerical integration.

6. Results

In this chapter, Race Time Difference results are presented for different wheel-tire combinations. These are presented together with the Race Time Difference expectation from the sensitivity analysis. The averages of the Race Time Differences for each race are also presented. The Race Time Difference is calculated by subtracting the Simulated Original Race Times from the Simulated Race Times. Lastly, the results from an experiment with added weight to C60 wheels is presented. All simulations are only performed for 26mm tires because the 28mm and 30mm tires have a larger C_{rr} and weigh more than the 26mm, without offering any quantitative benefits for race times produced by the simulations.

6.1 Race time & Sensitivity results

In Table 6.1, the Race Time Differences for the simulation for different wheel-tire combinations can be seen, as well as the expected Race Time Differences from the sensitivity analysis. The results in this table are for a single cyclist, the same cyclist as for which the sensitivity results are performed. To get the results shown in the table, the Simulated Original Race Time is subtracted from the Simulated Race Time for each wheel-tire combination. For Brugge and Paris, the Simulated Original Race Time is produced using the tubular C60 wheel-tire combination. For Catalunya and Valencia, the Simulated Original Race Time is produced using the tubular C36 wheel-tire combination. Any result smaller than 0 in this table indicated that the cyclist was faster than the Simulated Original Race Time.

Brugge 26mm	C36	C50	C60	C36TL	C50TL	C60TL
Sensitivity expectation	38.09s	18.26s	0s	-80.83s	-100.61s	-118.89s
Simulation result	30.32s	13.41s	0s	-86.51s	-101.18s	-115.2s
Catalunya 26mm	C36	C50	C60	C36TL	C50TL	C60TL
Sensitivity expectation	0s	-10.03s	-17.76s	-80.60s	-90.20s	-98.18s
Simulation result	0s	-10.56s	-20.73s	-76.91s	-89.01s	96.33s
Paris 26mm	C36	C50	C60	C36TL	C50TL	C60TL
Sensitivity expectation	29.77s	14.20s	0s	-43.35s	-58.84s	-73.07s
Simulation result	21.92s	9.94s	0s	-48.56s	-60.73s	-72.47s
Valencia 26mm	C36	C50	C60	C36TL	C50TL	C60TL
Sensitivity expectation	0s	-12.55s	-22.95s	-81.66s	-93.88s	-104.47s
Simulation result	0s	-11.15s	-23.32s	-79.10s	-92.34s	-103.68s

Table 6.1: Table which shows the Race Time Differences and the expected Race Time Differences. For Brugge and Paris, Simulated Original Race Time is produced using C60 tubular wheels. For Valencia and Catalunya, Simulated Original Race Time is produced using C36 tubular wheels. A result smaller than 0 indicates that a cyclist was faster than the original components

The Race Time Differences for each individual cyclist can be seen in Table 6.2. These Race Time Differences are then averaged to show the average Race Time Differences for each race for the different wheel-tire combinations. These averages are shown in Table 6.3. The Simulated Race Times can be seen in Appendix C, Table C.1, C.2, C.3 and C.4.

Brugge 26mm	C36	C50	C60	C36TL	C50TL	C60TL
Cyclist 1	29.0s	11.4s	0s	-103.7s	-121.3s	-135.7s
Cyclist 2	30.3s	13.4s	0s	-86.5s	-101.2s	-115.2s
Cyclist 3	28.2s	12.5s	0s	-95.2s	-110.1s	-121.8s
Cyclist 4	26.0s	11.3s	0s	-96.4s	-111.8s	-123.1s
Cyclist 5	26.1s	13.7s	0s	-85.2s	-99.6s	-114.0s
Cyclist 6	29.8s	14.2s	0s	-98.5s	-112.9s	-127.6s

Catalunya 26mm	C36	C50	C60	C36TL	C50TL	C60TL
Cyclist 1	0s	-10.6s	-20.7s	-76.9s	-89.0s	-96.3s
Cyclist 2	0s	-11.5s	-22.6s	-67.6s	-80.4s	-88.9s

Paris 26mm	C36	C50	C60	C36TL	C50TL	C60TL
Cyclist 1	22.0s	11.0s	0s	-54.7s	-65.8s	-77.0s
Cyclist 2	21.9s	9.9s	0s	-48.6s	-60.7s	-72.5s
Cyclist 3	21.9s	11.6s	0s	-57.5s	-67.9s	-77.8s
Cyclist 4	21.4s	10.1s	0s	-47.1s	-57.6s	-68.0s
Cyclist 5	19.1s	10.1s	0s	-47.6s	-57.6s	-66.0s
Cyclist 6	19.9s	9.3s	0s	-40.5s	-51.4s	-61.1s

Valencia 26mm	C36	C50	C60	C36TL	C50TL	C60TL
Cyclist 1	0s	-11.2s	-23.3s	-79.1s	-92.3s	-103.7s
Cyclist 2	0s	-11.2s	-22.6s	-91.1s	-104.2s	-115.3s
Cyclist 3	0s	-12.8s	-23.3s	-78.4s	-90.9s	-100.3s

Table 6.2: Table that shows the Race Time Differences between components for each individual cyclist in Brugge, Catalunya, Paris and Valencia, for 26mm tires.

	C36	C50	C60	C36TL	C50TL	C60TL
Brugge	28.23s	12.74s	0s	-94.25s	-109.48s	-122.91s
Catalunya	0s	-11.03s	-21.68s	-72.27s	-84.69s	-92.64s
Paris	21.05s	10.35s	0s	-49.34s	-60.17s	-70.38s
Valencia	0s	-11.72s	-23.07s	-82.89s	-95.80s	-106.45s

Table 6.3: Table that shows the average Race Time Differences for all races, for all different wheel-tire combinations. This Race Time Difference is calculated by subtracting the Simulated Original Race Time from the Simulated Races Times for all different wheel-tire combinations.

6.2 Added weight experiment

Team DSM wanted to know how much lighter or heavier a wheel would need to be in order for the different wheels to have the same performance. This way, Team DSM would be able to make a more quantified request to manufacturers with their wishes for wheel specifications. In order to evaluate this, the "added weight experiment" is performed using the simulation.

The expected added extra mass in order to attain a 26mm C60 tubular wheel-tire combination, that has the same Simulated Race Time as a 26mm C36 tubular wheel-tire combination can be seen in Table 6.4. To obtain this, the sensitivity results from Table 5.3 are used. Table 6.4 also shows the simulated time difference between this (weighted) C60 wheel and the C36. This means that for the simulation using the C60 wheel, the same properties are used as for any C60 simulation. However, the mass of the wheel has the expected mass from Table 6.4 added. To calculate the "Difference C60" as it can be seen in the table, the C36 Simulated Race Time is subtracted from the (weighted) C60 Simulated Race Time. It is chosen to make the C60 heavier instead of making the C36 lighter because the sensitivity results on Brugge and Paris would have resulted in a negative wheel weight when making the C36 lighter.

	Brugge	Catalunya	Paris	Valencia
Expected mass	$+15.24kg$	$+0.44kg$	$+9.02kg$	$+0.70kg$
C36 race time	$17132.4s$	$16537.0s$	$12532.4s$	$16097.2s$
C60* race time	$17185.2s$	$16542.8s$	$12558.1s$	$16104.4s$
Difference C60* and C36	$52.8s$	$5.8s$	$26.7s$	$7.2s$

Table 6.4: Table which shows the expected mass that needs to be added in order to produce the same race results for C60 wheels as for C36 wheels. This table also shows the simulated race time for C36 and C60*. The Simulated Race Time for C60* is larger than predicted. **The C60 used for the simulation has the same properties as any C60, except for the mass. The expected mass from this table is added to produce the Simulated Race Time.*

7. Discussion

In this chapter, the results from Chapter 6 are discussed. Race Time Differences for different wheel-tire combinations are discussed. Along with where these Race Time Differences originate from and what the consequences of these Race Time Differences are. The results are used to answer the research question and sub-questions.

7.1 Race time & sensitivity

In Table 6.1, the expected Race Time Differences are shown together with the Race Time Differences. It can be seen that the expected Race Time Differences give a good indicator of what the Race Time Differences are going to be. However, there are small differences between expected Race Time Differences and the actual Race Time Differences. The sensitivity analysis, on which the expected Race Time Differences are based, is done by calculating the derivative for small parameter changes. When the differences in the parameter values are larger, this sensitivity analysis becomes less accurate. For these races however, the same conclusions about which wheel-tire combination is fastest can be drawn from the expected Race Time Differences as well as the actual Race Time Differences. This suggests that instead of running each wheel-tire combination, a sensitivity analysis can be performed to give a prediction of which wheel-tire combination would be the fastest. In Table 6.1, it can also be seen that the C60 tubeless wheel-tire combination is the fastest in all cases. In this table, it can be seen as well that the C36 tubular wheel-tire combination is the slowest in every case. Using the uncertainty from Chapter 5 (Table 5.5), it can be seen that the Race Time Differences for the C50 rims compared to the C36 and C60 rims are smaller than two times the potential error in the measurements (for both tubular and tubeless). Therefore, it cannot be confidently said that the C50 is faster than the C36 and slower than the C60. The Race Time Differences between C60 and C36 is greater than twice the potential error, so it can be confidently said that the C60 rims are faster than the C36 rims.

7.2 Different aspects of race time differences

Using the sensitivity per parameter as presented in Chapter 5, Table 5.6, the importance of each individual parameter can be seen. In the following subsections, the consequences of differences in these parameters is discussed.

7.2.1 Importance of aerodynamics and rolling resistance

When looking at Table 5.6, it can be seen that the stake of the C_DA is so high that this overrules the downsides of bringing a heavier and more aerodynamic wheel. Even with the drag reduction due to drafting in the peloton taken into account, the benefits of aerodynamics outweigh the added weight of a more aerodynamic wheel.

The C_{rr} also has a large impact on Simulated Race Time results. From the results it is clear that benefits of the reduction in rolling resistance while using tubeless tires more than offset the the extra weight of using a tubeless system. The data that was used to attain the values for the C_{rr} did not have enough measurements to be able to say anything about the error in the measurements. It is recommended that C_{rr} measurements are performed again, with a larger amount of samples. If that is done, the error in the Simulated Race Time results for the C_{rr} can be quantified. Since the effect of the rolling resistance on the Simulated Race Times is large, this is an important part that is still missing. There are some hobbyists who report values twice the value for C_{rr} as provided by Team DSM [27]. A difference of twice this value would have major impacts on the simulation, and might change the recommendations for which tire type to use. This is why it is important to revisit the C_{rr} measurements and make sure that these are accurate and representative

7.2.2 Importance of Weight and Inertia

Table 5.6 shows the sensitivity results for Catalunya and Valencia. In this table, it can be seen that the sensitivity to extra weight is higher for these mountainous races. Using these sensitivity results, estimations can be done for how much weight needs to be added to a C60 wheel to make it perform similarly to a C36-set. The results of this weight-addition can be seen in table 6.4. It is expected that the simulation behaves similarly when subtracting weight instead of adding weight. As can be seen in Table 6.4, a C60 wheel-set with extra added mass is slower than a C36. Because the sensitivity results are based on a local derivative, these Simulated Race Time values will be different than predicted, for larger deviations from the base weight. The weight additions for Brugge and Paris are not realistic, no cycling wheel-set is going to be 9 or even $15kg$ heavier. However, a $440g$ and $700g$ decrease in weight of a wheel-set for Catalunya and Valencia, respectively, does not seem unattainable in the future. A C36 wheel set with a 19% and 31% weight reduction would outperform the C60's on Catalunya and Valencia, respectively. This estimation does not take the change in rotational inertia for a weight increase/reduction into account, which is not correctly represented in this Thesis as already discussed in Chapter 5. When a realistic effect of the rotational inertia is implemented, a smaller weight reduction can have the same effect.

7.2.3 Individual differences

When looking at Table 6.2, the individual Race Time Differences show different race time gains and losses for individual cyclists. No clear connection could be found between power, weight and wind which would explain these individual differences clearly. This could be due to the fact that the cyclists currently have a generic value for C_DA. Assuming this C_DA represents the average cyclist, in reality, lighter cyclists would be skinnier as well, resulting in a smaller frontal area and most likely in a smaller C_DA. On the other hand, a heavier cyclist would most likely have a larger frontal area and thus a larger C_DA than given right now. This difference between the estimated C_DA and the real C_DA of the cyclist distorts the image of the individual Race Time Differences. If the actual C_DA of the cyclist is smaller than the C_DA which is assigned to them for the simulation, this cyclist will experience smaller wind speeds in the current simulation. The wind calculation would make up for the lack of power the cyclist would have to overcome the aerodynamic drag force since the simulation will find a larger drag force than the cyclist experienced in the real world. Since it is not really know whether the real C_DA is actually smaller or larger than the assigned C_DA for the simulation, the individual race time differences are distorted. A better estimate for C_DA for all individual cyclists might result in clearer relations between power, experienced wind and cyclist mass.

7.3 Conclusion

The first sub-question is: "What is the influence of the change in inertia, mass, rolling resistance and aerodynamic drag on the wheel-tire combination choice?" To answer this question: Inertia and mass have a relatively small impact on the wheel choice, especially in flatter courses. When the course becomes more mountainous, the impact of mass increases. This model does not correctly represent the effects of inertia. However, the impact of inertia is not expected to change the decision on which wheel-tire combination to use. Both the change aerodynamic drag and the change rolling resistance have a large impact on the wheel-tire choice. The impact of the change in aerodynamics is large enough to choose a C60 rim over a C36 rim in every situation analyzed. The change in rolling resistance between tubular and tubeless tire systems merits a change to tubeless in every situation. The uncertainty on this decision is not fully quantified. To verify this conclusion on the rolling resistance, extra information about the parameters is required.

The second sub-question was : "How reliable are the results of the simulation?". Chapter 5 shows the error estimation over the different aspects of a component change. It can be concluded that within a 95.4% confidence interval, a C60 rim is faster than a C36 rim. The C50 rim lies within the uncertainty of the measurements, so no conclusions can be confidently drawn from these results. The largest portion of the uncertainty originates from the values for C_DA. The uncertainty for the C_{rr} is not quantified. This is why nothing can be said about the reliability of the results for a tubular or tubeless tire system.

This leads into the main research question"What is the optimal cycling wheel-tire combination, available to Team DSM in order to ride different road cycling races as fast as possible?". With the current wheels that Team DSM has available, it is worth it to bring a heavier, more aerodynamic wheel when cycling a road cycling race. It is also worth it to bring a heavier, tubeless wheel that has a lower rolling resistance. The effect of the inertia is not yet correctly captured by this model, but it is not expected to change the

outcome of these simulations. In mountainous races, the extra weight brought about by using these more aerodynamic, tubeless wheels matters more. In the future, weight reductions to wheel-sets could tip the scales in favor of lighter wheels with less favorable aerodynamics in mountainous races. On flatter race courses, this is unlikely to happen. A weight reduction will not weigh up to the advantages of a tubeless tire system compared to a tubular tire system. Therefore, when using the information gathered from the simulations performed for this Thesis, a C60 tubeless wheel-tire combination is the optimal cycling wheel-tire combination for Team DSM.

8. Conclusions and Future recommendations

This chapter summarizes the conclusions of this thesis and highlights future recommendations for after this study.

8.1 Conclusions

This thesis quantifies the differences in performance between multiple cycling wheel-tire combinations to help Team DSM select the right combination for road cycling races. A model is constructed in order to evaluate this. This model forward simulates a cyclist over a race course, using race-data from Team DSM. From the results from these simulations, it is concluded that a C60 26mm Tubeless wheel-tire combination is the fastest option for each of the races analyzed. It is seen that the advantage of the better aerodynamics of a C60 wheel outweighs the extra weight of this wheel-type. The potential error on the measurements that were used to obtain the parameters for the model is large enough to not be able to say with certainty that C50 rims are faster than C36 rims and slower than C60 rims. It can be said confidently that C60 rims are faster than C36 rims.

A reduction of $700g$ in wheel-set weight of a C36 tubular wheel-set would cause the C36 to perform better than the C60 in both of the mountainous races analyzed. A reduction of $440g$ in wheel-set weight of a C36 tubular wheel-set would make the C36 perform better than the C60 in just one of the mountainous races analyzed. The benefit of a tubeless tire system greatly outweighs the downsides of a tubeless system being heavier. No prediction could be made for the uncertainty of the values of the C_{rr}.

A sensitivity analysis can function as a predictor for the performance of different cycling wheels during cycling road races. For this to work, the differences in weight, inertia, aerodynamics and rolling resistance between different wheel-tire combinations need to be sufficiently small.

8.2 Future recommendations

The model that is used, is a 2D model. The yaw angle of the incoming air has influence on the C_DA characteristics of a cyclist. That is why it could be valuable to expand this model to a 3D model which would be able to handle a variable yaw, to get a more accurate approximation of the wind. One way to do this would be to also record the wind direction during a race. Using the different $C_DA's$ found in wind-tunnel testing, a variable C_DA could be assigned, depending on the yaw angle. Currently, this C_DA is an estimated value for a generic cyclist. Since every cyclist is different in terms of power output, weight and frontal surface area, it would be more accurate to have a specific C_DA for each cyclist. This would of course be very resource intensive and would probably only be worth it for one of the top-cyclists for a team, or when a 3D model has been constructed. An intermediate approach for this to mitigate this drawback, would be to first start with generalizing cyclists into cyclists with a small C_DA, medium C_DA and a larger C_DA.

The values that are currently used for C_{rr} should be revisited. The current values used are based on experimental results with at most 2 data points. This makes it difficult to evaluate the uncertainty of the rolling resistance. Having more data points available for these measurements would help to determine the actual impact of the rolling resistance. When these measurements for the C_{rr} are revisited, it could be valuable to try to obtain a surface-specific C_{rr}. Tires have a different interaction with different surfaces. Different tire pressures could be beneficial on one road surface, but cost more energy on another road surface. Having surface-specific rolling resistance, one could determine the best overall tire pressure or tire type for a race, even with greatly varying road surfaces.

As discussed in Chapter 5, the determination of the braking force should be improved. Currently, some turns are missed, and from the sensitivity results it can be seen that not enough braking is applied. This can possibly be fixed with a different turn identification algorithm. However, an even more accurate

solution would be to add a sensor to the bicycle that registers whether the cyclist is braking. Ideally, this would also register the braking force. Even if only the time stamps and locations of when and where the cyclist brakes were registered, this would already greatly help to improve the braking protocol. When the implementation of the braking force implementation is improved, it would be interesting to see if it matters how windy the course is for the choice of wheel. The current model allows the speed to be different from the original racing speed. In reality, this race speed would be imposed by the peloton. Allowing the speed to vary, decreases the importance of aerodynamic components since the drag force is dependent on the sum of the speed of the rider and the wind speed. If the wind speed increases, the speed of the rider decreases. This allows for a smaller aerodynamic drag increase than would be the case if the speed of the cyclist was forced.

This model also has other uses that could be exploited in the future. Where it is now used to evaluate different wheel sets, it would also be able to accommodate the comparison of different components than just wheels. This model could assist in making choices for anything that is a consideration between aerodynamics and weight on races. An example of this could be helmets, brakes, clothing, etc. It would also be interesting to run this model for a range of different constant powers and wind-speeds for different cyclists and courses. In this way, it can be explored whether there is a cyclist-specific tipping point to choose between using more aerodynamic components or lighter components. It could also be beneficial to run many races to build a database, which could show whether there is a correlation between the race length and altitude for choice of components. With all these runs it would be able to build a database which could possibly show what components to choose when given the length and the altitude gain for that race.

9. Acknowledgements

I would like to express my deepest appreciation to my chair and daily supervisor dr. J.K. Moore for his invaluable patience and feedback, my supervisors from Team DSM, ir. H. Ubbens and P. Rooijakkers for the insights and expertise knowledge on professional cycling and my committee-member Prof. dr. D.J. Veeger for spending time and energy supporting my graduation.

I'm also gratefull to all of the members of the bicycle-lab. From them, I received a warm welcome, fun people to talk to and good insights. My thanks also goes out to my girlfriend, who supported me throughout this process and proofread this entire document.

Lastly, I'd like to mention my friends and family who have been very supportive during the completion of this Thesis.

Bibliography

[1] F. Mutter and T. Pawlowski, "Role models in sports - can success in professional sports increase the demand for amateur sport participation?" *Sport Management Review*, vol. 17, pp. 324–336, 3 2014, ISSN: 14413523. DOI: 10.1016/j.smr.2013.07.003.

[2] F. Mutter and T. Pawlowski, "The causal effect of professional sports on amateur sport participation, an instrumental variable approach," *International Journal of Sport Finance*, vol. 9, pp. 172–188, 2014.

[3] E. Heinen, K. Maat, and B. van Wee, "The effect of work-related factors on the bicycle commute mode choice in the netherlands," *Transportation*, vol. 40, pp. 23–43, 1 Jan. 2013, ISSN: 15729435. DOI: 10.1007/s11116-012-9399-4.

[4] B. S. Noble, "Is elite sport a driver for medical advance?" *Sporto mokslas / Sport Science*, vol. 1, pp. 2–7, 83 Apr. 2016, ISSN: 1392-1401. DOI: 10.15823/sm.2016.1.

[5] C. J. Ringuet-Riot, A. Hahn, and D. A. James, "A structured approach for technology innovation in sport," *Sports Technology*, vol. 6, pp. 137–149, 3 2013, ISSN: 19346190. DOI: 10.1080/19346182.2013.868468.

[6] E. Heinen, B. van Wee, and K. Maat, "Commuting by bicycle: An overview of the literature," *Transport Reviews*, vol. 30, pp. 59–96, 1 Jan. 2010, ISSN: 01441647. DOI: 10.1080/01441640903187001.

[7] O. Karte, "Vaker op de fiets? de effecten van overheidsmaatregelen," 2007.

[8] S. Roa and L. Muñoz, "Analysis of the bicycle change strategy for hilly time-trials," *Ingeniería y competitividad: revista científica y tecnológica*, vol. 20, pp. 53–61, 1 2018, ISSN: 0123-3033. DOI: 10.25100/iyc.v20i1.6179.

[9] G. P. Boswell, "Power variation strategies for cycling time trials: A differential equation model," *Journal of Sports Sciences*, vol. 30, pp. 651–659, 7 Apr. 2012, ISSN: 02640414. DOI: 10.1080/02640414.2012.654397.

[10] E. Rømcke *et al.*, "Simulation model for road cycling time trials with a non-constant drag area," SciTePress, 2019, pp. 76–83, ISBN: 9789897583834. DOI: 10.5220/0008165800760083.

[11] S. D. Roa and L. E. Muñoz, "Bicycle change strategy for uphill time-trial races," *Proceedings of the Institution of Mechanical Engineers, Part P: Journal of Sports Engineering and Technology*, vol. 231, pp. 207–219, 3 Sep. 2017, ISSN: 1754338X. DOI: 10.1177/1754337117724310.

[12] F. Malizia, T. van Druenen, and B. Blocken, "Impact of wheel rotation on the aerodynamic drag of a time trial cyclist," *Sports Engineering*, vol. 24, 1 Dec. 2021, ISSN: 14602687. DOI: 10.1007/s12283-021-00341-6.

[13] G. Atkinson, O. Peacock, and L. Passfield, "Variable versus constant power strategies during cycling time-trials: Prediction of time savings using an up-to-date mathematical model," *Journal of Sports Sciences*, vol. 25, pp. 1001–1009, 9 Jul. 2007, ISSN: 02640414. DOI: 10.1080/02640410600944709.

[14] D. M. Fintelman, M. Sterling, H. Hemida, and F. X. Li, "Optimal cycling time trial position models: Aerodynamics versus power output and metabolic energy," *Journal of Biomechanics*, vol. 47, pp. 1894–1898, 8 Jun. 2014, ISSN: 18732380. DOI: 10.1016/j.jbiomech.2014.02.029.

[15] A. Zignoli, "Influence of corners and road conditions on cycling individual time trial performance and 'optimal' pacing strategy: A simulation study," *Proceedings of the Institution of Mechanical Engineers, Part P: Journal of Sports Engineering and Technology*, vol. 235, pp. 227–236, 3 Sep. 2021, ISSN: 1754338X. DOI: 10.1177/1754337120974872.

[16] G. Atkinson and A. Brunskill, "Pacing strategies during a cycling time trial with simulated headwinds and tailwinds," *Ergonomics*, vol. 43, no. 10, pp. 1449–1460, 2000. DOI: 10.1080/001401300750003899.

[17] P. Cangley, L. Passfield, H. Carter, and M. Bailey, "The effect of variable gradients on pacing in cycling time-trials," *International Journal of Sports Medicine*, vol. 32, pp. 132–136, 2 2011, ISSN: 01724622. DOI: 10.1055/s-0030-1268440.

[18] S. A. Fayazi, N. Wan, S. Lucich, A. Vahidi, and G. Mocko, "Optimal pacing in a cycling time-trial considering cyclist's fatigue dynamics," Institute of Electrical and Electronics Engineers Inc., 2013, pp. 6442–6447, ISBN: 9781479901777. DOI: 10.1109/acc.2013.6580849.

[19] B. Blocken *et al.*, "Aerodynamic drag in cycling pelotons: New insights by cfd simulation and wind tunnel testing," *Journal of Wind Engineering and Industrial Aerodynamics*, vol. 179, pp. 319–337, Aug. 2018, ISSN: 01676105. DOI: 10.1016/j.jweia.2018.06.011.

[20] C. R. Kyle, "Reduction of wind resistance and power output of racing cyclists and runners travelling in groups," *Ergonomics*, vol. 22, pp. 387–397, 4 1979, ISSN: 13665847. DOI: 10.1080/00140137908924623.

[21] J. P. Broker, C. Kyle, R. Chester, and B. E. R., "Racing cyclists power requirements ins the 4000-m individual and team pursuits," *Medicine and Schience in Sports and Excercise*, vol. 31, pp. 1677–1685, 11 Nov. 1999.

[22] T. Defraeye *et al.*, "Cyclist drag in team pursuit: Influence of cyclist sequence, stature, and arm spacing," *Journal of Biomechanical Engineering*, vol. 136, 1 Jan. 2014, ISSN: 01480731. DOI: 10.1115/1.4025792.

[23] N. Barry, D. Burton, J. Sheridan, M. Thompson, and N. A. Brown, "Aerodynamic drag interactions between cyclists in a team pursuit," *Sports Engineering*, vol. 18, pp. 93–103, 2 Jun. 2015, ISSN: 14602687. DOI: 10.1007/s12283-015-0172-8.

[24] K. Shirasaki, K. Yamanobe, K. Akashi, and W. Takashima, "Variation of the drafting effect on the trailing rider for different numbers of riders in a cycling group," *Proceedings of the Institution of Mechanical Engineers, Part P: Journal of Sports Engineering and Technology*, p. 175 433 711 773 661, Nov. 2017, ISSN: 1754-3371. DOI: 10.1177/1754337117736617.

[25] B. Blocken, T. van Druenen, Y. Toparlar, and T. Andrianne, "Aerodynamic analysis of different cyclist hill descent positions," *Journal of Wind Engineering and Industrial Aerodynamics*, vol. 181, pp. 27–45, Oct. 2018, ISSN: 01676105. DOI: 10.1016/j.jweia.2018.08.010.

[26] M. Ling. (2022), [Online]. Available: https://www.theproscloset.com/blogs/news/pros-and-cons-of-tubeless-road-bike-tires.

[27] J. Bierman. (2022), [Online]. Available: https://www.bicyclerollingresistance.com/road-bike-reviews.

[28] J. Huang. (2020), [Online]. Available: https://cyclingtips.com/2020/02/whats-faster-tubes-or-tubeless-the-answer-remains-the-same-it-depends/.

[29] D. de Boer, TU Delft, 2022.

[30] K. Dahn, L. Mai, J. Poland, and C. Jenkins, "Frictional resistance in bicycle wheel bearings," *Cycling science*, 1991.

[31] H. Trenchard, "The complex dynamics of bicycle pelotons," University of Victoria, 2012. [Online]. Available: www.letour.fr,.

[32] T. van Druenen and B. Blocken, "Aerodynamic analysis of uphill drafting in cycling," *Sports Engineering*, vol. 24, 1 Dec. 2021, ISSN: 14602687. DOI: 10.1007/s12283-021-00345-2.

[33] P. Virtanen *et al.*, "SciPy 1.0: Fundamental Algorithms for Scientific Computing in Python," *Nature Methods*, vol. 17, pp. 261–272, 2020. DOI: 10.1038/s41592-019-0686-2.

[34] U. P. V. 1. OER Servicies. "Physical pendulum." (2022), [Online]. Available: https://courses.lumenlearning.com/suny-osuniversityphysics/chapter/15-4-pendulums/.

[35] S. S. Systems, "Crs43 technical datasheet." [Online]. Available: https://www.siliconsensing.com/products/gyroscopes/crs43/.

[36] Geokov. "Utm - universal transverse mercator." (2014), [Online]. Available: http://geokov.com/education/utm.aspx.

[37] T. I. B. B. can Andel T. Bieniek, "Bidirectional utm-wgs84 converter for python," [Online]. Available: https://github.com/Turbo87/utm.

[38] A. Goldschmidt, "Python derivative 0.4.2," [Online]. Available: https://pypi.org/project/derivative.

[39] J. R. Chasnov, "Numerical methods for engineers," 2020.

[40] G. W. E. H. S. P. Norsett, *Solving Ordinary Differential Equations I*. Springer Berlin Heidelberg, 1993. DOI: 10.1007/978-3-540-78862-1.

Appendices

A. Appendix A, rotational inertia measurements

A.1 Method 2 "Spinning Method"

An alternative method to measure the mass moment of inertia is to mount the wheel in such a way that it can spin freely. This can be in a upside down bike for example. A lightweight rope can be attached, which in turn runs over the circumference of the rim or tire. When this weight is released, this weight will pull down the wheel, giving the wheel a (near) constant acceleration. Using the forces shown in Figure A.1, an expression for the rotational inertia of the wheel can be determined.

summing the torques around the wheel, the following is found: $\Sigma\tau = I\alpha$. Where τ is the torque around the wheel axis, I is the rotational inertia and α is the angular acceleration. The tension force (F_T) can be determined by looking at the sum of the forces in the y-direction, $\Sigma F_{y_{mass}} = Ma_y = F_{g_{mass}} - F_T$ so $F_T = F_{g_{mass}} - Ma_y$ with $F_{g_{mass}} = Mg$

The torque can be expressed as $\tau = F_T L$. Also, a_y can be expressed in terms of the angular acceleration $a_y = L\alpha$ so Equation A.1 should be valid for the rotational inertia measured for the wheel.

$$I_{spin} = \frac{LM(g - L\alpha)}{\alpha} \tag{A.1}$$

A.2 Uncertainty of Both Methods

2 expressions were found to determine the mass moment of inertia of the bicycle wheels. To decide which method to choose, a prediction of the accuracy of these measurements is made.

Both measurement methods have in common that a length will have to be measured and a mass will have to be determined. For the measurement error, we take half the resolution of the measurement device. This gives $u_L = 0.0005m$ as the uncertainty for a good quality measuring tape. This reasoning also gives $u_m = 0.0005kg$ as uncertainty for a scale that shows the accuracy to a gram.

For the first method, a "Silicon Sensing Systems C43-02" would be used, which is an angular rate sensor. This device has an angular speed linear error is reported to be 0.002% [35]. So $u_\omega = 0.002\% \cdot \omega$. For the second method, a linear accelerometer is used, for which the accuracy is unknown. For now, it is assumed that the accuracy of the linear accelerometer is the same as the accuracy of the angular rate sensor $u_\alpha = 0.002\% \cdot \alpha$

In order to compare the reliability of the 2 methods, an estimation of the error estimation is calculated. Both methods have 3 terms with uncertainties, for which $u_{I_{pendulum,1}}$, $u_{I_{pendulum,2}}$, $u_{I_{pendulum,3}}$, $u_{I_{spin,1}}$, $u_{I_{spin,2}}$ and $u_{I_{spin,3}}$ are calculated. Here, it is known that:

$$u_{I_{pendulum}} = \sqrt{u^2_{I_{pendulum,1}} + u^2_{I_{pendulum,2}} + u^2_{I_{pendulum,3}}} \tag{A.2}$$

and

$$u_{I_{spin}} = \sqrt{u^2_{I_{spin,1}} + u^2_{I_{spin,2}} + u^2_{I_{spin,3}}} \tag{A.3}$$

The three different uncertainties for the rotational inertia that is measured with the pendulum method can be expressed as follows:

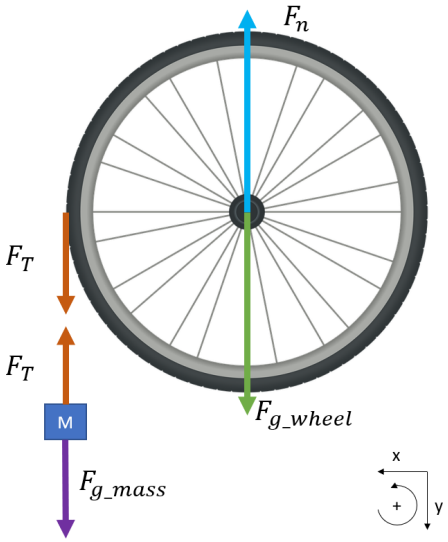

Figure A.1: Depiction of the forces that would be acting on the wheel in the spinning test for the inertia measurement. $F_{g_{wheel}}$ is the gravity force on the wheel from the mass of the wheel, F_n is the reaction force to this gravity force, F_T is the tension in the rope and $F_{g_{mass}}$ is the gravitation force on the mass, which is suspended from the wheel.

$$u_{I_{pendulum,1}} = |\frac{\delta I_{pendulum}}{\delta L}|u_L = |\frac{mg}{\omega^2} - 2mL|u_L \tag{A.4}$$

$$u_{I_{pendulum,2}} = |\frac{\delta I_{pendulum}}{\delta m}|u_m = |\frac{gL}{\omega^2} - L^2| \tag{A.5}$$

$$u_{I_{pendulum,3}} = |\frac{\delta I_{pendulum}}{\delta T}|u_T = | - 2\frac{mgL}{\omega^3}|u_\omega \tag{A.6}$$

We can do the same for the uncertainties on the rotational inertia for the spinning method.

$$u_{I_{spin,1}} = |\frac{\delta I_{spin}}{\delta L}| = |\frac{Mg}{\alpha} - 2LM|u_L \tag{A.7}$$

$$u_{I_{spin,2}} = |\frac{\delta I_{spin}}{\delta M}| = |\frac{Lg}{\alpha} - L^2|u_M \tag{A.8}$$

$$u_{I_{spin,3}} = |\frac{\delta I_{spin}}{\delta \alpha}| = | - \frac{Mg}{\alpha^2}|u_\alpha \tag{A.9}$$

When assuming a hanging mass on the spinning wheel of $M = 0.2kg$, using a rim radius of $L = 0.311m$ and estimate a inertia ($I = ML^2 = 0.0580kgm^2$), an estimate of an order of magnitude of the acceleration is gained, in order to give an estimation of the error propagation. These numbers give this estimate as $\alpha = 7.8859rad/s^2$. Including an estimate of $m = 0.700kg$ for the mass of the wheel and after timing with a stopwatch with 10 oscillations, an estimate of $\omega = 4.8rad/s$ is used. All this combined nets an estimation for the errors as follows:

$$u_{I_{pendulum}} = 2.44 \cdot 10^{-4} \tag{A.10}$$

$$u_{I_{spin}} = 1.87 \cdot 10^{-4} \tag{A.11}$$

A.3 Measurement Method Decision

As can be seen in Equation A.10 and Equation A.11, there is a difference in the error propagation of factor 1.3 in favor of the pendulum method, but this is subject to the parameters used. This method also does not take into account that there is friction in the suspension point of the pendulum method, friction in the bearings of the axis during the spinning method and also the weight of the rope in the spinning method. Even though these friction terms are not taken into account, both methods are considered to be accurate enough. A factor of 1.3 is not convincing enough to choose the pendulum method over the spinning method since the bearing friction was not taken into account, nor the weight of the rope or the friction at the suspension point. However, it could be challenging to ensure that the rope remains on the outer radius of the rim during the spinning method. This is why the pendulum method is chosen over the spinning method.

A.4 Rotational inertia results

This section shows the results of the "pendulum method" to measure the rotational inertia of the wheels. Figures A.2, A.3 and A.4 show these results in a bar graph. Table A.1 shows what the virtual additional weight of a wheel would be if only the linear inertia is considered.

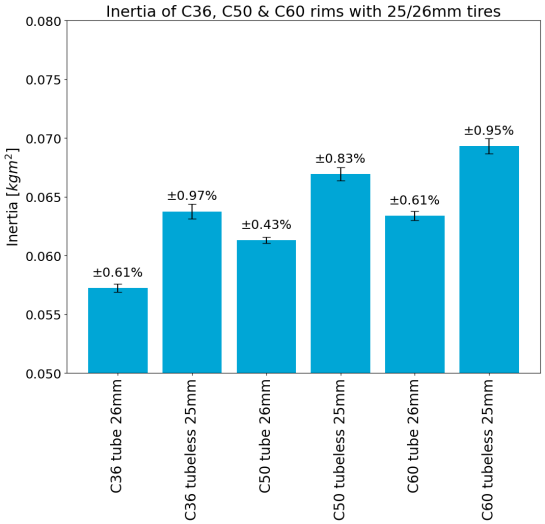

Figure A.2: In this figure you van see the inertia of all the possible rim-tire combinations with 25 and 26mm tires. In this graph you can also see the error bar which does not go over 1%. The reason that some error bars are significantly larger than others, is because that is a rim-tire combination which was not explicitly tested, which increases the uncertainty on the inertia

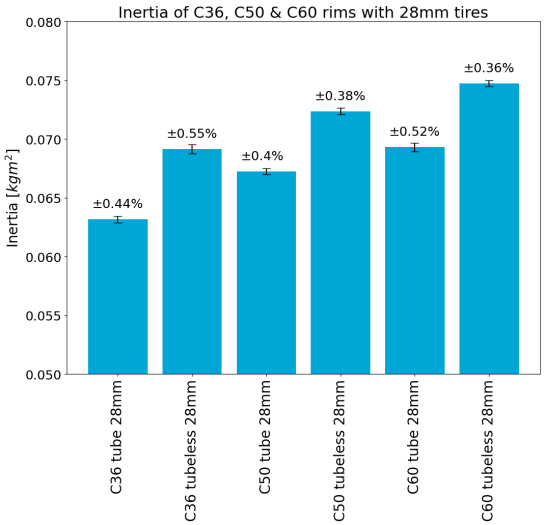

Figure A.3: In this figure you van see the inertia of all the possible rim-tire combinations with 28mm tires. In this graph you can also see the error bar which does not go over 1%. The reason that some error bars are significantly larger than others, is because that is a rim-tire combination which was not explicitly tested, which increases the uncertainty on the inertia

	Inertia (kgm^2)	Inertia/radius^2 (kg)
C36 26mm tubular	0.0572537	0.59
C36 26mm tubeless	0.0637566	0.65
C36 28mm tubular	0.0631683	0.63
C36 28mm tubeless	0.0691641	0.70
C50 26mm tubular	0.0613236	0.66
C50 26mm tubeless	0.0669526	0.72
C50 28mm tubular	0.0672382	0.66
C50 28mm tubeless	0.0723611	0.72
C60 26mm tubular	0.0634008	0.69
C60 26mm tubeless	0.0693239	0.75
C60 28mm tubular	0.06934008	0.72
C60 28mm tubeless	0.0747324	0.77
Rear Hub	0.0025063	0.026

Table A.1: Inertia and inertia divided by radius for each rim-tire combination used

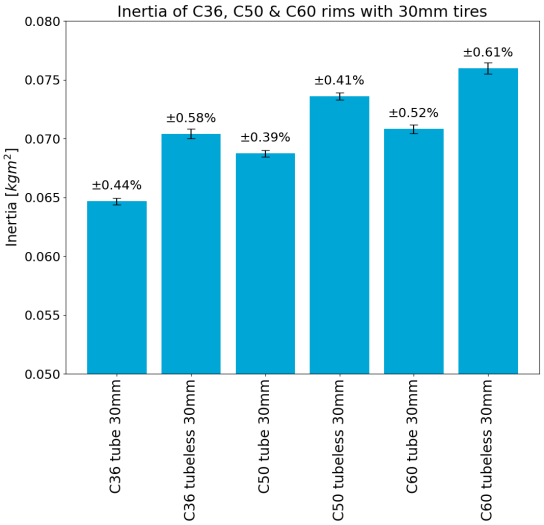

Figure A.4: In this figure you van see the inertia of all the possible rim-tire combinations with 30mm tires. In this graph you can also see the error bar which does not go over 1%. The reason that some error bars are significantly larger than others, is because that is a rim-tire combination which was not explicitly tested, which increases the uncertainty on the inertia

B. Appendix B, supplemental materials for numerical methods

This appendix shows supplemental materials for the numerical methods used in this Thesis. This includes constants, helmet choices for races, C_DA values and derivation of the C_DA differences that are used.

B.1 General Parameters

In Table B.1, Team DSMs' choice for helmets for different races can be seen. Table B.5 shows the weight of these helmets, among with the weight of other components. Table B.3 shows more constants that are used for the numerical simulation. Table B.4 shows the individual body weights of the cyclists.

B.2 Aerodynamic parameters

This section shows the percentage of time spent in different yaw-angles that Team DSM determined in Table B.6. Combining the information in this table with the C_DA measurements in Table B.7, the values in Table 4.4 are found for a one-dimensional wind speed..

Race	Helmet type
Brugge	Scott Cadence
Catalunya	Scott Centric
Brugge	Scott Cadence
Valencia	Scott Centric

Table B.1: Table that shows the helmet choice for each race analysed

	Inertia (kgm^2)	Weight (kg)	CdA difference
C36 26mm tubular	0.0572537	0.989	
C36 26mm tubeless	0.0637566	1.068	
C36 28mm tubular	0.0631683	1.015	
C36 28mm tubeless	0.0691641	1.087	
C50 26mm tubular	0.0613236	1.061	
C50 26mm tubeless	0.0669526	1.139	
C50 28mm tubular	0.0672382	1.087	
C50 28mm tubeless	0.0723611	1.158	
C60 26mm tubular	0.0634008	1.13	
C60 26mm tubeless	0.0693239	1.216	
C60 28mm tubular	0.06934008	1.156	
C60 28mm tubeless	0.0747324	1.235	
Rear hub	0.0025063	0.326	

Table B.2: Rim-tire specific inertia and CdA parameters used for running simulations

	Value
Radius wheel	$0.311m$
Air density	$1.225kg/m^3$
Gravitational constant	$9.81m/s^2$
Starting CdA	0.29025
Uphill CdA	0.35475
Downhill CdA	0.24725

Table B.3: General parameters used for running simulations

Rider nr.	Brugge	Catalunya	Paris	Valenica
1	$80.8kg$	$71.6kg$	$74.7kg$	$71.3kg$
2	$73.7kg$	$68.2kg$	$79.8kg$	$79.6kg$
3	$71.3kg$	$-kg$	$82.7kg$	$65.4kg$
4	$72.9kg$	$-kg$	$70.7kg$	$-kg$
5	$66.6kg$	$-kg$	$74.2kg$	$-kg$
6	$83.0kg$	$-kg$	$72.1kg$	$-kg$

Table B.4: Body weights of all the cyclists of which we have race-data from Team DSM

B.3 Wind

Table B.8 shows how often the solution for the wind wants to go to infinity.

B.3.1 Wind validation

Before the race data is fed into step 1 of the flow chart (4.1), a validation of this wind calculation is performed. In order to do this, a test-route is created. On this test-route, a cyclist is simulated as a point mass, similar to the model described in Chapter 2. First, the cyclist is simulated with a known, constant wind speed. This produces physically consistent results for power, speed and time. Using these results, it is checked whether the wind speed that was fed into this model can be recovered by the wind calculation. In Figure B.2, the original wind and the calculated wind are plotted. After a initial few metres, the solution converges to the the original wind. To do this validation, a 15km route was used. This route has a sinusoidal elevation profile of amplitude $200m$, one period long. A constant power of $200W$ and a constant wind speed of -$2m/s$ were used. The properties of the simulated cyclist can be found in Table B.9. The elevation and speed profile can be seen in Figure B.1

What	Weight (kg)	What	Weight(kg)
Bicycle frame	4.6	C60 Front rim	0.804
Clothing	0.86	C60 TL Front rim	0.896
Scott Centric	0.25	C60 Rear rim	1.130
Scott Cadence	0.28	C60 TL rear rim	1.222
C36 Front rim	0.633	26mm tire	0.326
C36 TL Front rim	0.748	26mm TL tire	0.320
C36 Rear rim	0.959	28mm tire	0.352
C36 TL rear rim	1.074	28mm TL tire	0.339
C50 Front rim	0.735	30mm tire	0.379
C50 TL Front rim	0.819	30mm TL tire	0.345
C50 Rear rim	1.061		
C50 TL rear rim	1.145		

Table B.5: Table which shows the weight of all the possible different components that could be used during a race.

Yaw	0-1.25°	1.25-3.75°	3.75-6.25°	6.25-8.75°	8.75-11.25°
Percentage of time spent	11.8%	27.1%	25.0%	19.2%	16.9%

Table B.6: Table which shows how long each cyclist spends on average in each yaw angle (data taken from technical report Team DSM).

Yaw angle	-10°	-7.5°	-5°	-2.5°	0
C36 26mm	0,09672719	0,096406069	0,097142528	0,096557962	0,096497082
C36 28mm	0,097662754	0,096779342	0,098008217	0,097269921	0,0968139
C50 26mm	0,094324095	0,094670196	0,096063614	0,09576077	0,095203676
C50 28mm	0,095291612	0,095637234	0,097355977	0,096902127	0,096149604
C60 26mm	0,095306893	0,095607116	0,09772093	0,097081539	0,0959174
C60 28mm	0,095746737	0,0959269	0,09727118	0,096833715	0,09621036

Yaw angle	2.5°	5°	7.5°	10°
C36 26mm	0,097316022	0,098325568	0,100485923	0,098958316
C36 28mm	0,097470019	0,098255692	0,099675089	0,098846166
C50 26mm	0,095304059	0,095700582	0,096703773	0,094647324
C50 28mm	0,09716809	0,097663976	0,098699097	0,097001206
C60 26mm	0,095685255	0,095712925	0,095814739	0,093054616
C60 28mm	0,09679391	0,096740521	0,09799907	0,094407171

Table B.7: CdA measured from wind tunnel sweeps for different wheel tire combinations on a road bicycle without a rider. We took a look at how much time a cyclist spends in each yaw-angle (Table B.6) and used that as weights to come to a 2D CdA difference for each rim (C36, C50 and C60). Those value can be seen in Table 4.4

Race	Nr. of moments where V_{wind} to -inf or +inf
Brugge 1	57
Brugge 2	55
Brugge 3	47
Brugge 4	47
Brugge 5	49
Brugge 6	51
Catalunya 1	114
Catalunya 2	137
Catalunya 3	200
Catalunya 4	102
Paris 1	13
Paris 2	12
Paris 3	13
Paris 4	16
Paris 5	21
Paris 6	19
Valencia 1	48
Valencia 2	55
Valencia 3	52
Valencia 4	49
Valencia 5	52

Table B.8: Table that shows how often the solution for the wind goes to -inf or +inf and is replaced by $-V$

Parameter	Value
m	$80kg$
g	$9{,}81m/s$
C_{rr}	0.007
C_dA	0.6325
ρ	$1.225kg/m^3$
I	$0.8kgm^2$
r	$0.311m$
Δt	$0.1s$

Table B.9: Parameters used for wind validation

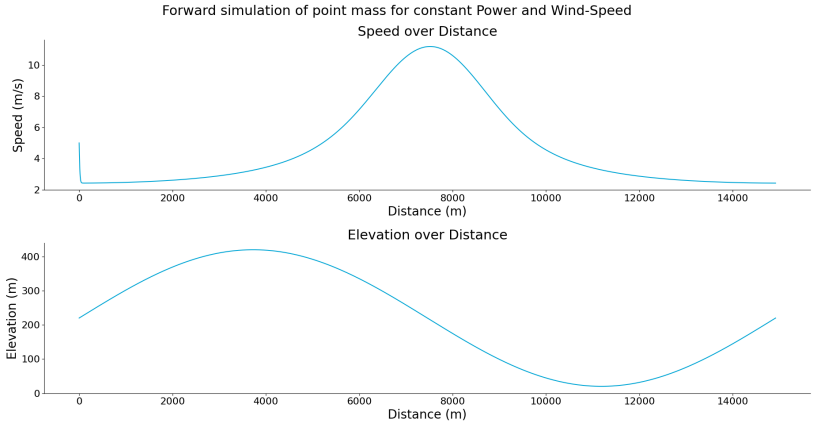

Figure B.1: Figure in which the speed over the given elevation profile can be seen. The power used to get this speed profile, is a constant $200W$ and the wind-speed was a constant -$2m/s$.

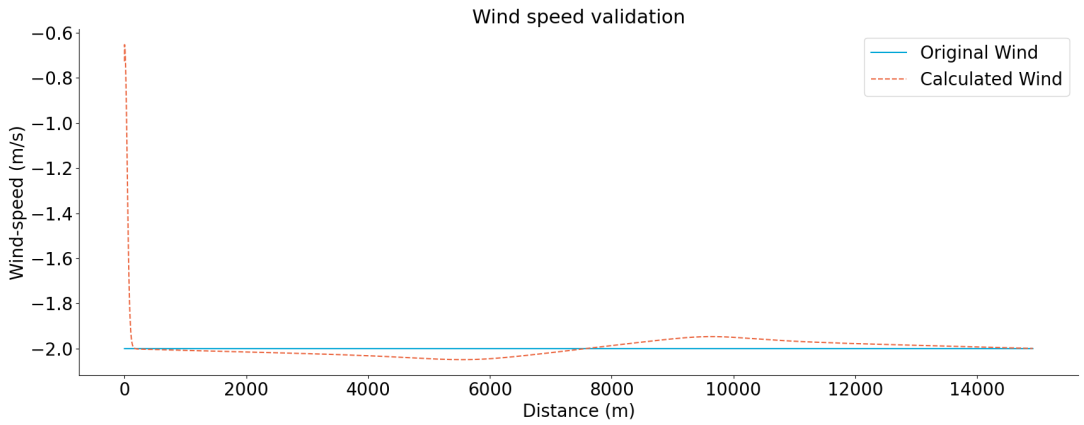

Figure B.2: Figure that shows a plot of the original wind and the calculated wind for the wind-validation.

C. Appendix C, simulation results

Tables C.1, C.2, C.3 and C.4 show the simulated race times for different wheel combinations with a 26mm tire for all the different races.

Brugge 26mm	C36	C50	C60	C36TL	C50TL	C60TL
Cyclist 1	17253.3s	17235.7s	17224.3s	17120.6s	17103.1s	17088.6s
Cyclist 2	17132.4s	17115.5s	17102.1s	17015.6s	17000.9s	16986.9s
Cyclist 3	17162.6s	17146.9s	17134.4s	17039.2s	17024.3s	17012.6s
Cyclist 4	17088.4s	17073.6s	17062.4s	16966.0s	16950.6s	16939.3s
Cyclist 5	17258.4s	17245.9s	17232.3s	17147.1s	17132.7s	17118.3s
Cyclist 6	17166.9s	17151.4s	17137.2s	17038.7s	17024.3s	17009.6s

Table C.1: Table that shows the simulated race time for each cyclist in Brugge for different wheel-tire combinations. TL means tubeless, and no addition to the combination means it is a tubular tire.

Catalunya 26mm	C36	C50	C60	C36TL	C50TL	C60TL
Cyclist 1	16537.0s	16526.5s	16516.3s	16460.1s	16448.0s	16440.7s
Cyclist 2	16203.3s	16191.8s	16180.7s	16135.6s	16122.9s	16114.3s

Table C.2: Table that shows the simulated race time for each cyclist in Catalunya for different wheel-tire combinations. TL means tubeless, and no addition to the combination means it is a tubular tire.

Paris 26mm	C36	C50	C60	C36TL	C50TL	C60TL
Cyclist 1	12894.4s	12883.4s	12872.4s	12817.6s	12806.6s	12795.3s
Cyclist 2	12532.5s	12520.5s	12510.5s	12462.0s	12449.8s	12438.1s
Cyclist 3	12450.1s	12439.8s	12428.2s	12370.7s	12360.2s	12350.3s
Cyclist 4	12946.0s	12934.8s	12924.6s	12877.5s	12867.0s	12856.7s
Cyclist 5	12250.7s	12241.7s	12231.6s	12184.0s	12174.0s	12165.7s
Cyclist 6	12420.4s	12409.7s	12400.4s	12359.9s	12349.0s	12339.4s

Table C.3: Table that shows the simulated race time for each cyclist in Paris for different wheel-tire combinations. TL means tubeless, and no addition to the combination means it is a tubular tire.

Valencia 26mm	C36	C50	C60	C36TL	C50TL	C60TL
Cyclist 1	16097.2s	16086.1s	16073.9s	16018.1s	16004.9s	15993.6s
Cyclist 2	16103.9s	16092.7s	16081.2s	16012.8s	15999.7s	15988.6s
Cyclist 3	15943.8s	15931.0s	15920.5s	15865.3s	15852.9s	15843.4s

Table C.4: Table that shows the simulated race time for each cyclist in Valencia for different wheel-tire combinations. TL means tubeless, and no addition to the combination means it is a tubular tire.